RSS Tech. Report 110398 Issued: November 3, 1998

Algorithm Theoretical Basis Document (ATBD)

AMSR Ocean Algorithm

Principal Investigator: Frank J. Wentz

Prepared for:
EOS Project
Goddard Space Flight Center
National Aeronautics and Space Administration
Greenbelt MD 20771

Prepared by:

Remote Sensing Systems
438 First Street, Suite 200, Santa Rosa, CA 95401 (707) 545-2904

Table of Contents

List of Figures

List of Tables

List of Symbols

Symbol	Definition	Units
a_{O1}, a_{O2}	coefficients for oxygen absorption	see Table 4
a_{V1}, a_{V2}	coefficients for water vapor absorption	see Table 4
a_{L1}, a_{L2}	coefficients for liquid water absorption	see Table 6
$\mathbf{A}$	the **A**-matrix relating **Y** to **X**	arbitrary
A_O	vertically integrated oxygen absorption	naper
A_V	vertically integrated water vapor absorption	naper
A_L	vertically integrated cloud liquid water absorption	naper
b_0 to b_7	coefficients for effective air temperature	see Table 4
c	speed of light	cm/s
C	chlorinity of sea water	parts/thousand
E	sea-surface emissivity	none
f	fractional foam coverage	none
F	foam+diffraction factor for sea-surface reflectivity	none
h	Planck's constant in eq. (2)	erg-s
h	height above Earth surface, elsewhere	cm
h_0	surface roughness length	cm
$\mathbf{h_i}$, $\mathbf{h_s}$	h-pol vectors for incident and scattered radiation	none
I_λ	specific intensity	erg/s-cm^3-ster
j	$\sqrt{-1}$	none
k	Boltzmann's constant	erg/K
$\mathbf{k_i}$	upward unit propagation vector	none
$\mathbf{k_s}$	downward unit propagation vector	none
L	vertically integrated cloud liquid water	mm
m_1, m_2	coefficients for foam+diffraction factor	s/m
$\mathbf{n}$	unit normal vector for tilted surface facet	none
$\mathbf{P}$	column vector of geophysical parameters	varies
$P(S_u,S_c)$	probability density function of surface slope	none
P_λ	specific power	erg/s
$\mathbf{p}$	unit polarization vector	none

Symbol	Definition	Units
r_0 to r_3	coefficients for geometric optics	see Table 7
R	total sea-surface reflectivity	none
R_0	specular reflectivity	none
R_{clear}	foam-free sea-surface reflectivity	none
R_{geo}	geometric optics sea-surface reflectivity	none
$R_{\times}$	reflectivity of secondary intersection	none
s	path length in Section 2.2	cm
s	salinity, elsewhere	parts/thousand
S	total path length through atmosphere	cm
S_c	crosswind slope for tilted surface facet	none
S_u	upwind slope for tilted surface facet	none
t_S	sea-surface temperature	Celsius
T	temperature	K
T_B	brightness temperature	K
T_{BU}	upwelling atmospheric brightness temperature	K
T_{BD}	downwelling atmospheric brightness temperature	K
$T_{B\Omega}$	sky radiation scattered upward by Earth surface	K
$T_{B\uparrow}$	upwelling surface brightness temperature	K
$T_{B\downarrow}$	downwelling cold space brightness temperature	K
T_C	cold space brightness temperature	K
T_D	effective temperature for downwelling radiation	K
T_E	effective temperature of surface+atmosphere	K
T_S	sea-surface temperature	K
T_U	effective temperature for upwelling radiation	K
T_V	typical sea temperature for given water vapor	K
$\mathbf{v_i}$, $\mathbf{v_s}$	v-pol vectors for incident and scattered radiation	none
V	vertically integrated water vapor	mm
W	wind speed 10 m above sea surface	m/s
$\mathbf{X}$	column input vector	arbitrary
$\mathbf{Y}$	column output vector	arbitrary
$\tilde{\mathbf{Y}}$	measurement vector	arbitrary

Symbol	Definition	Units
α	total absorption coefficient	naper/cm
α_O	oxygen absorption coefficient	naper/cm
α_V	water vapor absorption coefficient	naper/cm
α_L	cloud liquid water absorption coefficient	naper/cm
β	diffraction factor for sea-surface reflectivity	none
γ	coefficients for wind direction variation of E	none
ΔS^2	total slope variance of sea surface	none
ε	T_B measurement error in Section 3	K
ε	complex dielectric constant of water, elsewhere	none
ε_∞	dielectric constant at infinite frequency	none
ε_S	static dielectric constant of sea water	none
ε_{S0}	static dielectric constant of distilled water	none
ε_ϕ	error in specifying wind direction	degree
ε_{Ts}	error in specifying sea-surface temperature	K
θ_i	incidence angle	degree
θ_s	zenith angle	degree
κ	reduction in sea-surface reflectivity due to foam	none
φ_i	azimuth angle for k_i	degree
φ_s	azimuth angle for k_s	degree
ϕ	wind direction relative to azimuth look direction	degree
λ	radiation wavelength	cm
λ_R	relaxation wavelength of sea water	cm
λ_{R0}	relaxation wavelength of distilled water	cm
μ	change in T_B w.r.t. incidence angle	K/degree
η	spread factor for relaxation wavelengths	none
Ω	fit parameter for sea surface scattering integral	none
$\mathbf{X}$	error correlation matrix	arbitrary
ρ_h	h-pol Frensel reflection coefficient	none
ρ_v	v-pol Frensel reflection coefficient	none
ρ_L	liquid water density	g/cm^3
ρ_V	water vapor density	g/cm^3

Symbol	Definition	Units
ρ_o	density of water	g/cm^3
σ	ionic conductivity of sea water	s^{-1}
$\sigma_{o,c}$	co-pol. normalized radar cross section	none
$\sigma_{o,\times}$	cross-pol. normalized radar cross section	none
τ	atmospheric transmission	none
ν	radiation frequency	GHz
χ	shadowing function	none
$\Im$	linearizing function for T_B's	none
$\Re$	linearizing function for geophysical parameters	none

1. Overview and Background Information

1.1. Introduction

With the advent of well-calibrated satellite microwave radiometers, it is now possible to obtain long time series of geophysical parameters that are important for studying the global hydrologic cycle and the Earth's radiation budget. Over the world's oceans, these radiometers simultaneously measure profiles of air temperature and the three phases of atmospheric water (vapor, liquid, and ice). In addition, surface parameters such as the near-surface wind speed, the sea-surface temperature, and the sea ice type and concentration can be retrieved. A wide variety of hydrological and radiative processes can be studied with these measurements, including air-sea and air-ice interactions (i.e., the latent and sensible heat fluxes, fresh water flux, and surface stress) and the effect of clouds on radiative fluxes. The microwave radiometer is truly a unique and valuable tool for studying our planet.

This Algorithm Theoretical Basis Document (ATBD) focuses on the Advanced Microwave Scanning Radiometer (AMSR) that is scheduled to fly in December 2000 on the NASA EOS-PM1 platform. AMSR will measure the Earth's radiation over the spectral range from 7 to 90 GHz. Over the world's oceans, it will be possible to retrieve the four important geophysical parameters listed in Table 1. The rms accuracies given in Table 1 come from past investigations and on-going simulations that will be discussed. Rainfall can also be retrieved, which is discussed in a separate AMSR ATBD.

We are confident that the expected retrieval accuracies for wind, vapor, and cloud will be achieved. The Special Sensor Microwave Image (SSM/I) has already demonstrated these accuracies can be obtained. The AMSR wind retrievals will probably be more accurate than that of SSM/I and less affected by atmospheric moisture. However, with regards to the sea-surface temperature retrieval, we do have some concerns which are discussed in Section 1.5.

Table 1. Expected Retrieval Accuracy for the Ocean Products

Geophysical Parameter	Rms Accuracy
Sea-surface temperature T_S	0.5 K
Near-surface wind speed W	1.0 m/s
Vertically integrated (i.e., columnar) water vapor V	1.0 mm
Vertically integrated cloud liquid water L	0.02 mm

1.2. Objectives of Investigation

There are two major objectives of this investigation. The first is to develop an ocean retrieval algorithm that will retrieve T_S, W, V, and L to the accuracies specified in Table 1. These products will be of great value to the Earth science community. The second objective is to improve the radiative transfer model (RTM) for the ocean surface and non-raining atmosphere. The 6.9 and 10.7 GHz channels on AMSR will provide new information on the RTM at low frequencies. Experience has shown that these two objectives are closely linked.

A better understanding of the RTM leads to more accurate retrievals. A better understanding of the RTM also leads to new remote sensing techniques such as using radiometers to measure the ocean wind vector.

1.3. Approach to Algorithm Development

Radiative transfer theory provides the relationship between the Earth's brightness temperature T_B (K) as measured by AMSR and the geophysical parameters T_S, W, V, and L. This ATBD addresses the inversion problem of finding T_S, W, V, and L given T_B. We place a great deal of emphasis on developing a highly accurate RTM. Most of our AMSR work thus far has been the development and refinement of the RTM. This work is now completed, and Section 2 describes the RTM in considerable detail.

The importance of the RTM is underscored by the fact that AMSR frequency, polarization, and incidence angle selection is not the same as previous satellite radiometers. Table 2 compares AMSR with other radiometer systems. Albeit some of the differences are small, they are still significant enough to preclude developing AMSR algorithms by simply using existing radiometer measurements. The differences in frequencies and incidence angle must be taken into account when developing AMSR algorithms.

Table 2. Comparison of Past and Future Satellite Radiometer Systems

Radiometer	Frequencies/Polarization						Inc. Angle
SeaSat SMMR	6.6VH	10.7VH	18.0VH	21.0VH	37.0VH		49°
Nimbus-7 SMMR	6.6VH	10.7VH	18.0VH	21.0VH	37.0VH		51°
SSM/I			19.3VH	22.2V	37.0VH	85.5VH	53°
TRMM TMI		10.7VH	19.3VH	21.0VH	37.0VH	85.5VH	53°
PM AMSR	6.9VH	10.7VH	18.7VH	23.8VH	36.5VH	89.0VH	55°

Our approach uses the existing radiometer measurements to calibrate various components of the RTM. The RTM formulation then provides the means to compute T_B at any frequency in the 1-100 GHz range and at any incidence angle in the 50°-60° range. For the SSM/I frequencies and incidence angle, the resulting RTM is extremely accurate. It is able to reproduce the SSM/I T_B to a rms accuracy of about 0.6 K. (This figure comes from Table 3 in *Wentz* [1997], and represents the rms difference between the RTM and SSM/I observations after subtracting out radiometer noise and *in situ* inter-comparison errors.) As one moves away from the SSM/I frequencies and incidence angle, we do expect some degradation in the RTM accuracy. However, the hope is that the physics of the RTM is reliable enough so that this degradation is minimal when we interpolate/extrapolate to the AMSR configuration.

Given an accurate and reliable RTM, geophysical retrieval algorithms can be developed. We are developing in parallel two types of algorithms: the linear regression algorithm and the non-linear, iterative algorithm. Section 3 discusses each type of algorithm. For both types, the algorithm development is based on a simulation in which brightness temperatures for a wide variety of ocean scenes are produced by the RTM. These simulated T_B's then serve as both a training set and a test set for the algorithms. We have tested this simulation methodology by developing algorithms for SSM/I. These SSM/I algorithms are then tested using actual measurements. The results show that the SSM/I algorithms coming from the RTM simulation have essentially the same performance as those developed directly from SSM/I measurements. These results are not surprising since the RTM was calibrated to reproduce the SSM/I T_B's. This exercise is more of a closure verification of the techniques being used. Work on specifying the AMSR retrieval algorithm has just begun and some preliminary results are given in Section 3. In this upcoming year (1997), we will be doing many simulation tests and much more will be learned about algorithm performance.

1.4. Algorithm Development Plan

Figure 1 shows the four basic steps in developing the AMSR ocean algorithm. We are currently in the first phase of developing the β-version algorithm. One shortcoming of the β-version algorithm is that there is some uncertainty about the wind component of the RTM at 6.9 and 10.7 GHz. At these frequencies, we are using SeaSat SMMR T_B's collocated with SeaSat scatterometer winds to specify the wind component of the RTM [*Wentz et al.*,1986]. The SeaSat SMMR suffered from calibration problems, and we are concerned about the accuracy of the low-frequency wind component.

The next phase of algorithm development will begin when the TRMM radiometer (TMI) observations become available. TMI will provide well-calibrated 10.7-GHz ocean observations. With these observations, we will update the wind component of the RTM at 10.7 GHz. We will also investigate the possibility of retrieving T_S in the tropical oceans from 10.7 GHz, although we know that the AMSR 6.9 GHz channel will end up being superior. Of particular concern is the variation of the 10.7-GHz T_B with wind direction. Wind direction variability may be the dominate source of error in the T_S retrieval if the T_B wind direction signal is large.

The first AMSR will be launched aboard the ADEOS-2 spacecraft in 1999. This will provided a great opportunity to refine and test the AMSR ocean algorithm. The dependence of the sea-surface emissivity on temperature, wind speed, and wind direction can be precisely determined. Calibration data for the sea-surface temperature will be obtained from cloud-free IR temperature retrievals. Buoy winds and/or winds from the ADEOS-2 scatterometer (SeaWinds) will be used to calibrated the wind component of the AMSR algorithm. A thorough calibration/validation activity for the AMSR ocean algorithm will then conducted for the ADEOS-2 AMSR. Some final changes in the algorithm will probably be made, and the resulting algorithm will be delivered to NASA 6 months before the launch of the PM AMSR.

1.5. Concerns Regarding Sea-Surface Temperature Retrieval

The capability of measuring sea-surface temperature T_S through clouds has long been a goal of microwave radiometry. A global T_S product unaffected by clouds and aerosols would be of great benefit to both the scientific and commercial communities. AMSR will be the first satellite sensor to furnish this product, provided that certain requirements are met.

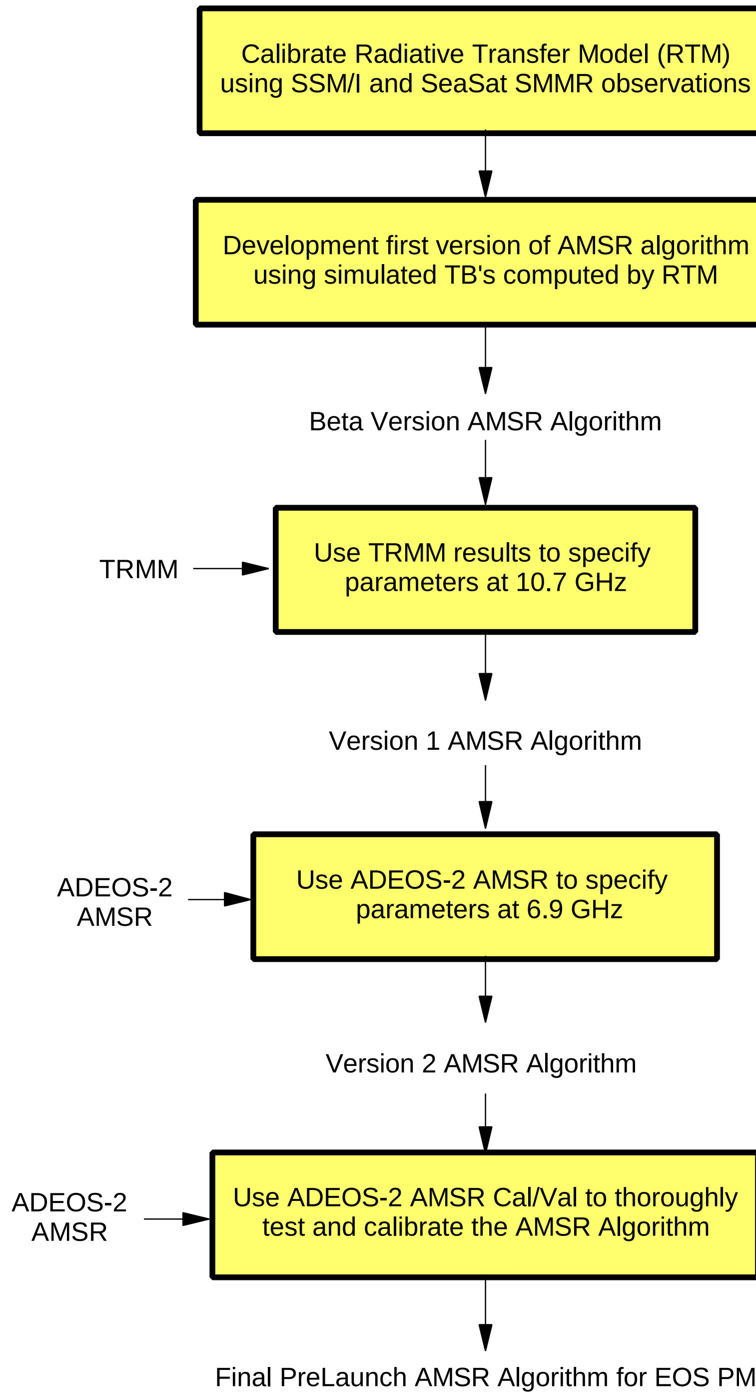

Fig. 1. Development steps for ocean algorithm

The retrieval of sea-surface temperature to an accuracy of 0.5 K requires the following:

1. Radiometer noise for the 6.9V channel be about 0.1K
2. Incidence angle be known to an accuracy of 0.05°
3. Radio frequency interference (RFI) be less than 0.1 K.
4. The retrieval algorithm be able to separate wind effects from T_S effects

The first two conditions will be satisfied if the AMSR instrument specifications are met. The radiometer noise figure for one 6.9 GHz observation is 0.3 K. However, the 6.9 GHz observations are greatly over sampled. Observations are taken every 10 km, but the spatial resolution of the footprint is 58 km. During the Level-1C processing, adjacent observations are averaged together in such a way as to reduce the noise to 0.1 K. In doing this averaging, the spatial resolution is degraded by only 2%. The pointing knowledge for the PM platform should be sufficient to meet the incidence angle requirement, as is discussed in Section 3.6.

The last two conditions are our major concern. The band from 5.9 to 7.8 GHz is allocated to various communication links. The possibility exists that the sidelobe transmissions from these links will contaminate the AMSR 6.9 GHz measurements. Clearly, this problem needs more attention. A survey of relevant communication links need to be made and sidelobe contamination calculations need to be done.

From an algorithm standpoint, the most difficult part of the T_S retrieval is separating the T_S signal from the wind signal. The T_B wind signal is due to both wind speed and wind direction variations. It is relatively easy to distinguish wind speed variations from a T_S variation. Wind speed mostly affects the h-pol channel and T_S mostly affects the v-pol channel. Thus the polarization signature of the observations provides the means to separate T_S from W. However, wind direction variations are more problematic in that both polarizations are affected. Simulations (see Section 3) show that without (with) wind direction variability, the T_S retrieval error is 0.3 (0.6). These results are contingent on the assumed amplitude for the wind directional T_B signal at 6.9 GHz. If the wind direction variation proves to be a dominant error source, then we will need to make a correction to the T_S retrieval based on some wind direction database, as is discussed in Section 4.3.

Note that in contrast to IR retrieval techniques, the atmospheric interference at 6.9 GHz is very small and easily removed using the higher frequency channels, except when there is rain. And, observations affected by rain are easily detected and can be discarded. Thus, the atmosphere does not pose a problem for the T_S retrieval.

1.6. Historical Perspective

In the 1960's, it was first recognized that microwave radiometers had the ability to measure atmospheric water vapor V and cloud liquid water L [*Barret and Chung*, 1962; *Staelin*; 1966]. In 1972, Nimbus-5 satellite was launched. Aboard Nimbus-5 was the Nimbus-E Microwave Spectrometer (NEMS), which had channels at 22.235 and 31.4 GHz. *Staelin et al.* [1976] and *Grody* [1976] demonstrated that water vapor and cloud water could indeed be retrieved from the NEMS T_B's. In these retrievals they ignored the effect of wind at the ocean surface; at these frequencies the effect of T_S is minimal.

In the years preceding the launch of Nimbus-5, there were several developments concerning the effect of wind at the ocean's surface. *Stogryn* [1967] developed a theory to account for the wind-induced roughness, and *Hollinger* [1971] made some radiometric measurements from a fixed tower to test the theory. He removed the most obvious foam effects from the data and found that the roughness effect was somewhat less than the Stogryn theory would predict by a frequency dependent factor. Using airborne data, *Nordberg et al.* [1971] characterized the combined foam and roughness effect at 19.35 GHz. At their measurement angle the observed effect was dominated by foam. Stogryn's geometric optics theory was extended to included diffraction effects, multiple scattering, and two-scale partitioning by *Wu and Fung* [1972] and *Wentz* [1975].

The first simultaneous retrieval of W, V, and L was based on airborne data from the 1973 joint US-USSR Bering Sea Experiment (BESEX) [*Wilheit and Fowler*, 1977]. Later *Chang and Wilheit* [1979] combined two NIMBUS-5 instruments, the ESMR and the NEMS for a W, V, and L retrieval. *Wilheit* [1979a] used the 37-GHz dual polarized data from the Electrically Scanned Microwave Radiomter (ESMR) to explore the wind-induced roughness of the ocean surface. This was later combined with other data to generate a semi-empirical model for the ocean surface emissivity [*Wilheit*, 1979b] in preparation for the 1978 launch of the Scanning Multichannel Microwave Radiometer (SMMR) on the Nimbus-7 and SeaSat satellites. A theory for the retrieval of all 4 ocean parameters was published by *Wilheit and Chang* [1980].

The launch of the SeaSat and Nimbus-7 SMMR's spurred many investigation on SMMR retrieval algorithms and model functions [*Wentz*, 1983; *Njoku and Swanson*, 1983; *Alishouse*, 1983; *Chang et al*, 1984; *Gloersen et al.*, 1984], and the state-of-the-art in oceanic microwave radiometry quickly advanced. It became clear that the water vapor retrievals were highly accurate. A major improvement in the wind retrieval was made when *Wentz et al.* [1986] combined the SeaSat SMMR T_B's and the SeaSat scatterometer (SASS) wind retrievals to develop an accurate, semi-empirical relationship for the wind-induced emissivity.

Sea-surface temperature retrievals have been less successful. The measurement of T_S requires relatively low microwave frequencies (4-10 GHz). The SMMR's were the first satellite sensors with the appropriate frequencies to retrieve T_S. However, the SMMR's suffered from a poor calibration design, and the reported T_S retrievals [*Njoku and Swanson*, 1983; *Milman and Wilheit*, 1985] were useful for little more than a demonstration of the possibility of T_S retrievals for future, better calibrated radiometers.

The next major milestone was the launch of the Special Sensor Microwave Imager (SSM/I) in 1987. In contrast to SMMR, SSM/I has an external calibration system that provides stable observations. Unfortunately, the lowest SSM/I frequency is 19.3 GHz, and hence T_S retrievals are not possible. Shortly after the launch, there was a flurry of new SSM/I algorithms. Most of these algorithms, such as the *Goodberlet et al.* [1989] wind algorithm and the *Alishouse et al.* [1990] vapor algorithm, were simply statistical regressions to *in situ* data (see Section 3.5). These algorithms performed reasonably well but provided no information on the relevant physics. A more physical approach to algorithm development for SSM/I was taken by *Schluessel and Luthardt* [1991] and *Wentz* [1992, 1997]. This physical approach to algorithm development is described herein and will be the basis for the AMSR ocean algorithm.

1.7. AMSR Instrument Characteristics

The PM AMSR instrument is similar to SSM/I. The major differences are that AMSR has more channels and a larger parabolic reflector. AMSR takes dual polarization observations (v-pol and h-pol) at the 6 frequencies shown in Table 3. The offset 1.6-m diameter parabolic reflector focuses the Earth radiation into an array of 6 feedhorns. The radiation collected by the feedhorns is then amplified by 14 separate total-power radiometers. The 18.7 and 23.8 GHz receivers share a feedhorn, while dedicated feedhorns are provided for the other frequencies. Two feedhorns are required for the 89 GHz channels to achieve a 5-km along-track spacing. Figure 2 shows the block diagram for this configuration.

The parabolic reflector and feedhorn array are mounted on a drum containing the radiometers, digital data subsystem, mechanical scanning subsystem, and power subsystem. The reflector/feed/drum assembly is rotated about the axis of the drum by a coaxially mounted bearing and power transfer assembly. All data, commands, timing and telemetry signals, and power pass through the assembly on slip ring connectors to the rotating assembly.

A cold reflector and a warm load are mounted on the transfer assembly shaft and do not rotate with the drum assembly. They are positioned off axis such that they pass between the feedhorn array and the parabolic reflector, occulting it once each scan. The cold reflector reflects cold sky radiation into the feedhorn array thus serving, along with the warm load, as calibration references for the AMSR.

The AMSR rotates continuously about an axis parallel to the spacecraft nadir at 40 rpm. At an altitude of 705 km, it measures the upwelling Earth brightness temperatures over an angular sector of ± 61° degrees about the sub-satellite track, resulting in a swath width of 1445 km. During a scan period of 1.5 seconds, the spacecraft sub-satellite point travels 10 km. Even though the instantaneous field-of-view for each channel is different, Earth observations are recorded at equal intervals of 10 km (5 km for the 89 GHz channels) along the scan. The two 89-GHz feedhorns are offset such that their two scan lines are separated by 5 km in the along-track direction. The nadir angle for the parabolic reflector is fixed at 47.4°, which results in an Earth incidence angle θ_i of 55° ± 0.3°. The small variation in θ_i is due to the slight eccentricity of the orbit and the oblateness of the Earth.

As compared to the PM AMSR. the AMSR to fly on the ADEOS-2 spacecraft has two additional frequencies: 50.3 and 52.8 GHz. The tables in Section 2 for the radiative transfer model include these two additional frequencies.

Table 3. Instrument Specifications for PM AMSR

Center Frequencies (GHz)	6.925	10.65	18.7	23.8	36.5	89.0
Bandwidth (MHz)	350	100	200	400	1000	3000
Sensitivity (K)	0.3	0.6	0.6	0.6	0.6	1.1
IFOV (km x km)	76 × 44	49× 28	28 × 16	31 × 18	14 × 8	6 × 4
Sampling Rate (km x km)	10 × 10	10 × 10	10× 10	10 × 10	10 × 10	5 × 5
Integration Time (msec)	2.6	2.6	2.6	2.6	2.6	1.3
Main Beam Efficiency (%)	95.3	95.0	96.3	96.4	95.3	96.0
Beamwidth (degrees)	2.2	1.4	0.8	0.9	0.4	0.18

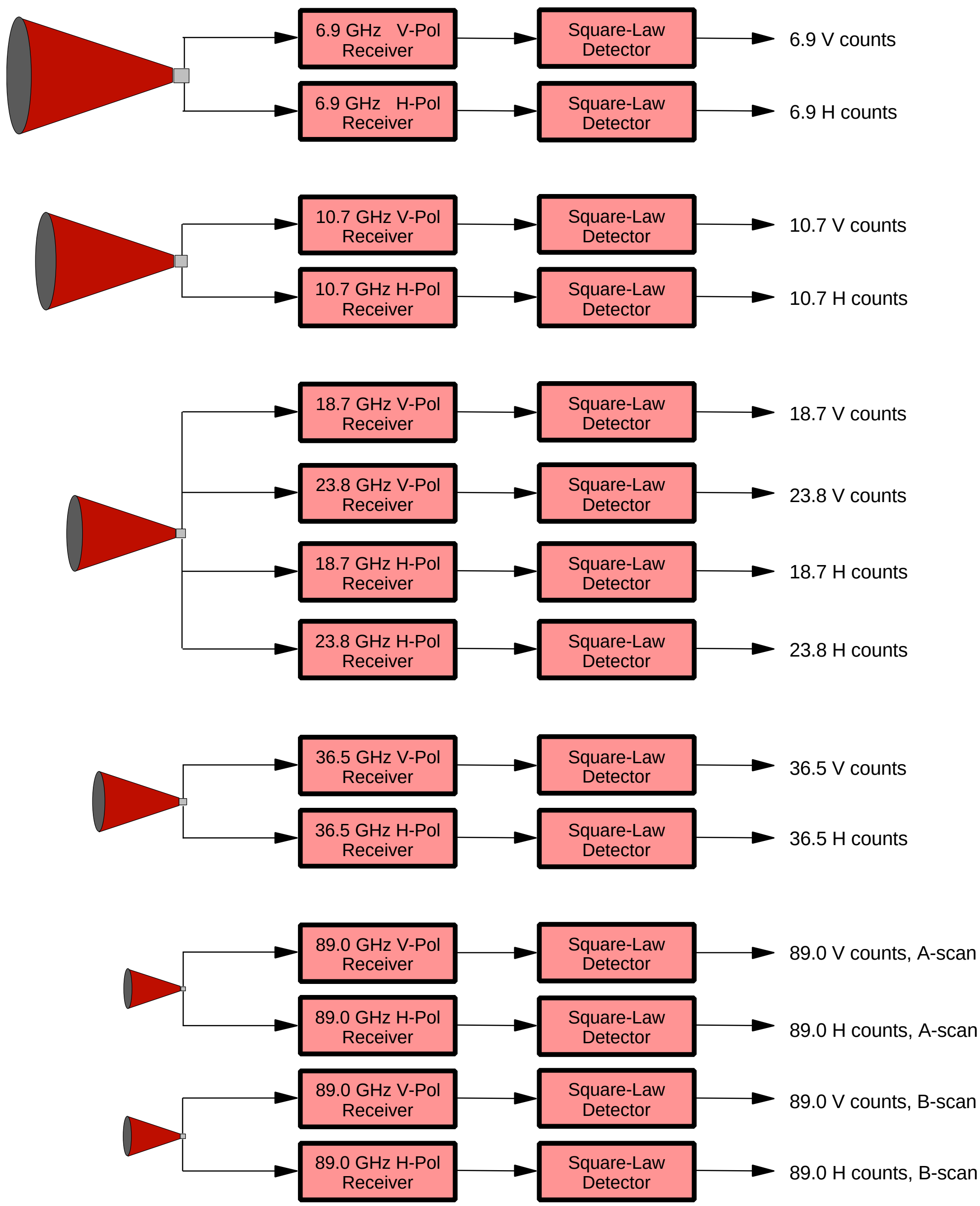

Fig. 2. Block diagram for PM AMSR feedhorns and radiometers.

2. Geophysical Model for the Ocean and Atmosphere

2.1. Introduction

The key component of the ocean parameter retrieval algorithm is the geophysical model for the ocean and atmosphere. It is this model that relates the observed brightness temperature (T_B) to the relevant geophysical parameters. In remote sensing, the specification of the geophysical model is sometimes referred to as the forward problem in contrast to the inverse problem of inverting the model to retrieve parameters. An accurate specification of the geophysical model is the crucial first step in developing the retrieval algorithm.

2.2. Radiative Transfer Equation

We begin by deriving the radiative transfer model for the atmosphere bounded on the bottom by the Earth's surface and on the top by cold space. The derivation is greatly simplified by using the absorption-emission approximation in which radiative scattering from large rain drops and ice particles is not included. Over the spectral range from 6 to 37 GHz, the absorption-emission approximation is valid for clear and cloudy skies and for light rain up to about 2 mm/h. The results of *Wentz and Spencer* [1997] indicate that only 3% of the SSM/I observations over the oceans viewed rain rates exceeding 2 mm/h. Thus, the absorption-emission model to be presented will be applicable to about 97% of the AMSR ocean observations.

In the microwave region, the radiative transfer equation is generally given in terms of the radiation brightness temperature (T_B), rather than radiation intensity. So we first give a brief discussion on the relationship between radiation intensity and T_B. Let P_λ denote the power within the wavelength range $d\lambda$, coming from a surface area dA, and propagating into the solid angle $d\Omega$. The specific intensity of radiation I_λ is then defined by

$$P_\lambda = I_\lambda \cos\theta_i \, d\lambda \, dA \, d\Omega \tag{1}$$

The specific intensity is in units of erg/s-cm^3-steradian. The angle θ_i is the incidence angle defined as the angle between the surface normal and the propagation direction. For a black body, I_λ is given by Planck's law to be [*Reif*, 1965]

$$I_\lambda = \frac{2hc^2}{\lambda^5\left[\exp(hc/\lambda kT) - 1\right]} \tag{2}$$

where c is the speed of light (2.998×10^{10} cm/s), h is Planck's constant (6.626×10^{-27} erg-s), k is Boltzmann's constant (1.381×10^{-16} erg/K), λ (cm) is the radiation wavelength, and T (K) is the temperature of the black body. Consider a surface that is emitting radiation with a specific intensity I_λ. Then the brightness temperature T_B for this surface is defined as the temperature at which a black body would emit the radiation having specific intensity I_λ. In the microwave region, the exponent in (2) is small compared to unity, and (2) can be easily inverted to give T_B in terms of I_ν.

$$T_B = \frac{\lambda^4 I_\lambda}{2kc} \tag{3}$$

This approximation is the well known Rayleigh Jeans approximation for $\lambda >> hc/kT$.

In terms of T_B, the differential equation governing the radiative transfer through the atmosphere is

$$\frac{\partial T_B}{\partial s} = -\alpha(s)\left[T_B(s) - T(s)\right] \tag{4}$$

where the variable s is the distance along some specified path through the atmosphere. The terms $\alpha(s)$ and $T(s)$ are the absorption coefficient and the atmospheric temperature at position s. Equation (4) is simply stating that the change in T_B is due to (1) the absorption of radiation arriving at s and (2) to emission of radiation emanating from s. We let s = 0 denote the Earth's surface, and let s = S denote the top of the atmosphere (i.e., the elevation above which $\alpha(s)$ is essentially zero).

Two boundary conditions that correspond to the Earth's surface at the bottom and cold space at the top are applied to equation (4). The surface boundary conditions states that the upwelling brightness temperature at the surface $T_{B\uparrow}$ is the sum of the direct surface emission and the downwelling radiation that is scattered upward by the rough surface [*Peake*, 1959].

$$T_{B\uparrow}(\mathbf{k_i},0) = E(\mathbf{k_i})T_S + \frac{\sec\theta_i}{4\pi}\int_0^{\pi/2}\sin\theta_s d\theta_s \int_0^{2\pi} d\varphi_s T_{B\downarrow}(\mathbf{k_s},0)\left[\sigma_{o,c}(\mathbf{k_s},\mathbf{k_i}) + \sigma_{o,\times}(\mathbf{k_s},\mathbf{k_i})\right] \tag{5}$$

where the first T_B argument denotes the propagation direction of the radiation and the second argument denotes the path length s. The unit propagation vectors $\mathbf{k_i}$ and $\mathbf{k_s}$ denote the direction of the upwelling and downwelling radiation, respectively. In terms of polar angles in a coordinate system having the z-axis normal to the Earth's surface, these propagation vectors are given by

$$\mathbf{k_i} = \left[\cos\varphi_i \sin\theta_i, \sin\varphi_i \sin\theta_i, \cos\theta_i\right] \tag{6a}$$

$$\mathbf{k_s} = -\left[\cos\varphi_s \sin\theta_s, \sin\varphi_s \sin\theta_s, \cos\theta_s\right] \tag{6b}$$

The first term in (5) is the emission from the surface, which is the product of the surface temperature T_S and the surface emissivity $E(\mathbf{k_i})$. The second term is the integral of downwelling radiation $T_{B\downarrow}(\mathbf{k_s})$ that is scattered in direction $\mathbf{k_i}$. The integral is over the 2π steradian of the upper hemisphere. The rough surface scattering is characterized by the bistatic normalized radar cross sections (NRCS) $\sigma_{o,c}(\theta_s,\theta_i)$ and $\sigma_{o,\times}(\theta_s,\theta_i)$. These cross sections specify what fraction of power coming from $\mathbf{k_s}$ is scattered into $\mathbf{k_i}$. The subscripts c and $\times$ denote co-polarization (i.e., incoming and outgoing polarization are the same) and cross-polarization (i.e., incoming and outgoing polarizations are orthogonal), respectively. The cross sections also determine the surface reflectivity $R(\mathbf{k_i})$ via the following integral.

$$R(\mathbf{k_i}) = \frac{\sec\theta_i}{4\pi}\int_0^{\pi/2}\sin\theta_s d\theta_s \int_0^{2\pi} d\varphi_s\left[\sigma_{o,c}(\mathbf{k_s},\mathbf{k_i}) + \sigma_{o,\times}(\mathbf{k_s},\mathbf{k_i})\right] \tag{7}$$

The surface emissivity $E(\mathbf{k_i})$ is given by Kirchhoff's law to be

$$E(\mathbf{k_i}) = 1 - R(\mathbf{k}_i) \tag{8}$$

It is important to note that equations (5) an (7) provide the link between passive microwave radiometry and active microwave scatterometry. The scatterometer measures the radar back-scatter coefficient, which is simply $\sigma_{o,c}(-\mathbf{k_i},\mathbf{k_i})$.

The upper boundary condition for cold space is

$$T_{B\downarrow}(\mathbf{k_s}, S) = T_C \tag{9}$$

This simply states that the radiation coming from cold space is isotropic and has a magnitude of T_C = 2.7 K.

The differential equation (4) is readily solved by integrating and applying the two boundary conditions (5) and (9). The result for the upwelling brightness temperature at the top of the atmosphere (i.e., the value observed by Earth-orbiting satellites) is

$$T_{B\uparrow}(\mathbf{k_i}, S) = T_{BU} + \tau\left[ET_S + T_{B\Omega}\right] \tag{10}$$

where T_{BU} is the contribution of the upwelling atmospheric emission, τ is the total transmittance from the surface to the top of the atmosphere, E is the Earth surface emissivity given by (8), and $T_{B\Omega}$ is the surface scattering integral in (5). The atmospheric terms can be expressed in terms of the transmittance function $\tau(s_1,s_2)$

$$\tau(s_1, s_2) = \exp\left\{-\int_{s_1}^{s_2} ds\ \alpha(s)\right\} \tag{11}$$

which is the transmittance between points s_1 and s_2 along the propagation path $\mathbf{k_s}$ or $\mathbf{k_i}$. The total transmittance τ in (10) is given by

$$\tau = \tau(0, S) \tag{12}$$

and the upwelling and downwelling atmosphere emissions are given by

$$T_{BU} = \int_0^S ds\ \alpha(s)\ T(s)\ \tau(s,S) \tag{13a}$$

$$T_{BD} = \int_0^S ds\ \alpha(s)\ T(s)\ \tau(0,s) \tag{13b}$$

The sky radiation scattering integral is

$$T_{B\Omega} = \frac{\sec\theta_i}{4\pi}\int_0^{\pi/2} \sin\theta_s d\theta_s \int_0^{2\pi} d\varphi_s (T_{BD} + \tau T_C)\left[\sigma_{o,c}(\mathbf{k_s}, \mathbf{k_i}) + \sigma_{o,\times}(\mathbf{k_s}, \mathbf{k_i})\right] \tag{14}$$

Thus, given the temperature T_S and absorption coefficient α at all points in the atmosphere and given the surface bistatic cross sections, T_B can be rigorously calculated. However, in practice, the 3-dimensional specification of T_S and α over the entire volume of the atmosphere is not feasible, and to simplify the problem, the assumption of horizontal uniformity is made. That is to say, the absorption is assumed to only be a function of the altitude h above the

Earth's surface, i.e., $\alpha(s) = \alpha(h)$. To change the integration variable from ds to dh, we note that for the spherical Earth

$$\frac{\partial s}{\partial h} = \frac{1+\delta}{\sqrt{\cos^2\theta + \delta(2+\delta)}} \tag{15}$$

where θ is either θ_i or θ_s, $\delta = h/R_E$, and R_E is the radius of the Earth. In the troposphere $\delta \ll 1$, and an excellent approximation for $\theta < 60°$ is,

$$\frac{\partial s}{\partial h} = \sec\theta \tag{16}$$

With this approximation and the assumption of horizontal uniformity, the above equations reduce to the following expressions.

$$\tau(h_1, h_2, \theta) = \exp\left[-\sec\theta \int_{h_1}^{h_2} dh\ \alpha(h)\right] \tag{17}$$

$$\tau = \tau(0, H, \theta_i) \tag{18}$$

$$T_{BU} = \sec\theta_i \int_0^H dh\ \alpha(h)\ T(h)\ \tau(h, H, \theta_i) \tag{19a}$$

$$T_{BD} = \sec\theta_s \int_0^H dh\ \alpha(h)\ T(h)\ \tau(0, h, \theta_s) \tag{19b}$$

Thus, the brightness temperature computation now only requires the vertical profiles of $T(h)$ and $\alpha(h)$ along with the surface cross sections. The following two sections discuss the atmospheric model for $\alpha(h)$ and the sea-surface model for the cross sections, respectively. In closing, we note that the AMSR incidence angle is 55° and hence approximation (16) is quite valid, with one exception. In the scattering integral, θ_s goes out to 90°, and in this case we use (15) to evaluate the integral.

2.3. Model for the Atmosphere

In the microwave spectrum below 100 GHz, atmospheric absorption is due to three components: oxygen, water vapor, and liquid water in the form of clouds and rain [*Waters*, 1976]. The sum of these three components gives the total absorption coefficient (napers/cm).

$$\alpha(h) = \alpha_O(h) + \alpha_V(h) + \alpha_L(h) \tag{20}$$

Numerous investigators have studied the dependence of the oxygen and water vapor coefficients on frequency ν (GHz), temperature T (K), pressure P (mb), and water vapor density ρ_V (g/cm^3) [*Becker and Autler*, 1946; *Rozenkranz,* 1975; *Waters*, 1976; *Liebe*, 1985]. To specify α_O and α_V as a function of (ν,T,P,ρ_V) we use the *Liebe* [1985] expressions with one modification. The self-broadening component of the water vapor continuum is reduced by a factor of 0.52 (see below). The liquid water coefficient α_L comes directly from the Rayleigh approximation to Mie scattering and is a function of T and the liquid water density ρ_L (g/cm^2)

(see below). Figure 3 shows the total atmospheric absorption for each component. Results for three water vapor cases (10, 30, and 60 mm) are shown. The cloud water content is 0.2 mm. This corresponds to a moderately heavy non-raining cloud layer.

Let A_I denote the vertically integrated absorption coefficient.

$$A_I = \int_0^H dh\ \alpha_I(h) \tag{21}$$

where h is the height (cm) above the Earth's surface and subscript I equals O, V, or L. Equations (17) and (18) then give the total transmittance to be

$$\tau = \exp\left[-\sec\theta_i \left(A_O + A_V + A_L\right)\right] \tag{22}$$

Assuming for the moment that the atmospheric temperature is constant, i.e., T(h) = T, then the integrals in equations (19) can be exactly evaluated in closed form to yield

$$T_{BU} = T_{BD} = (1-\tau)T \tag{23}$$

In reality, the atmospheric temperature does vary with h, typically decreasing at a lapse rate of about -5.5 C/km in the lower to mid troposphere. In view of (23), we find it convenient to parameterize the atmospheric model in terms of the following upwelling and downwelling effective air temperatures:

$$T_U = T_{BU} / (1-\tau) \tag{24a}$$

$$T_D = T_{BD} / (1-\tau) \tag{24b}$$

These effective temperatures are indicative of the air temperature averaged over the lower to mid troposphere. Note that in the absence of significant rain, T_U and T_D are very similar in value, with T_U being 1 to 2 K colder.

In view of the above equations, one sees that the atmospheric model can be parameterized in terms of the following 5 parameters:

1. Upwelling effective temperature T_U
2. Downwelling effective temperature T_D
3. Vertically integrated oxygen absorption A_O
4. Vertically integrated water vapor absorption A_V
5. Vertically integrated liquid water absorption A_L

To study the properties of the first four parameters, we use a large set of 42,195 radiosonde flights launched from small islands [*Wentz*, 1997]. These radiosonde reports provide air temperature T(h), air pressure p(h), and water vapor density $\rho_V(h)$ at a number of levels in the troposphere. From these data, the coefficients α_O and α_V are computed from the *Liebe* [1985] expressions, except that the water vapor continuum term is modified as discussed in the next paragraph. Performing the numerical integrations as indicated above, T_U, T_D, A_O, and A_V are found for each radiosonde flight. In addition, the vertically integrated water vapor V is also computed.

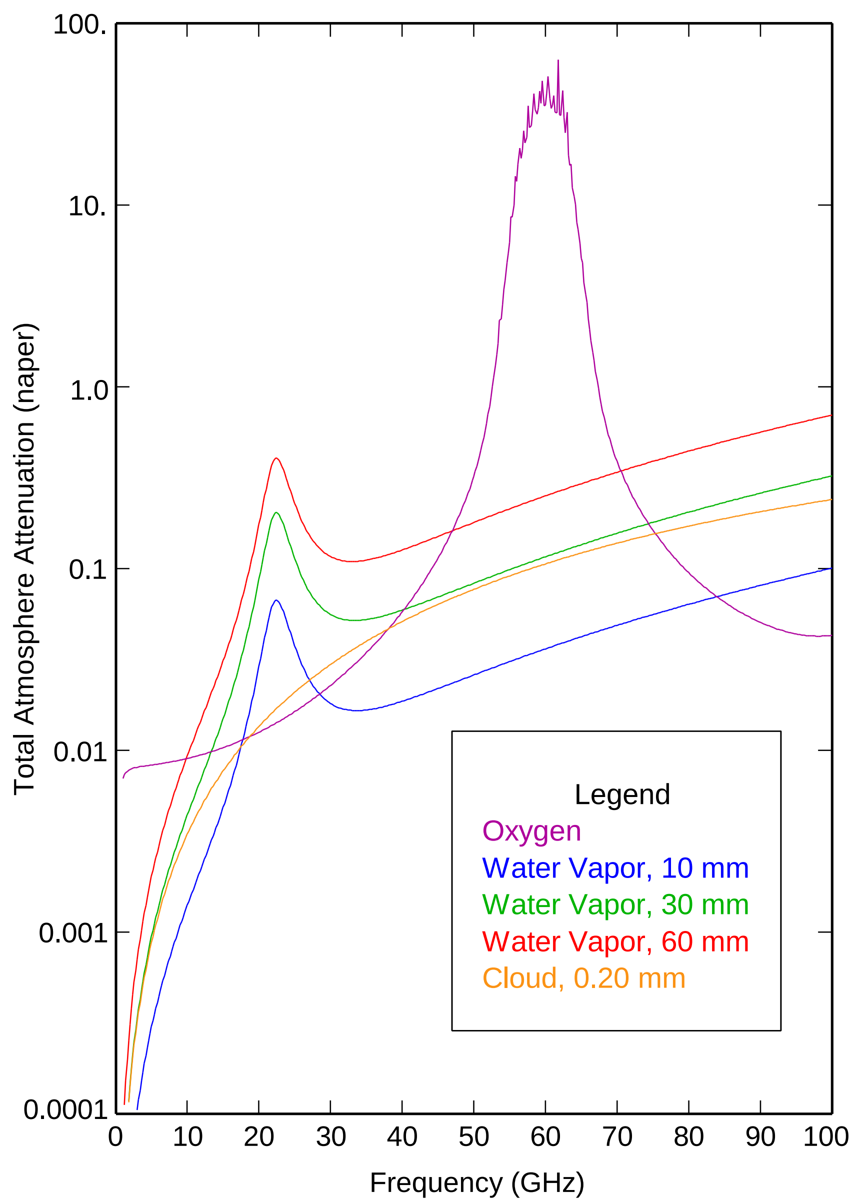

Fig. 3. The atmospheric absorption spectrum for oxygen, water vapor, and cloud water. Results for three water vapor cases (10, 30, and 60 mm) are shown. The cloud water content is 0.2 mm which corresponds to a moderately heavy non-raining cloud layer.

$$V = 10 \int_0^H dh\ \rho_V(h) \tag{25}$$

where $\rho_V(h)$ is in units of g/cm^3, and the leading factor of 10 converts from g/cm^2 to mm.

Wentz [1997] computed A_V directly from collocated SSM/I and radiosonde observations. At 19, 22, and 37 GHz, the Liebe A_V was found to be 4%, 3%, and 20% higher than the SSM/I-derived value, respectively. To quote *Liebe* [1985]: 'Water vapor continuum absorption has been a major source of uncertainty in predicting millimeter wave attenuation rates, especially in the window ranges.' The frequency of 37 GHz is in a water vapor window and is most affected by the continuum. It should be noted that Liebe also needed to rely on combined radiometer-radiosonde measurements to infer the continuum in the 6 to 37 GHz region. Liebe's data set in this spectral region is rather limited and does not contain any 37 GHz observations. We believe the SSM/I method of deriving A_V is more accurate than Liebe's method, and hence adjust the *Liebe* [1985] water vapor spectrum so that it will agree with the SSM/I results. We find that very good agreement is obtained by reducing the self-broadening component of the water vapor continuum by a factor of 0.52. After this adjustment, the agreement at all three frequencies is within ± 1%.

Figure 4 shows the T_D values computed from the 42,195 radiosondes plotted versus V. Three frequencies are shown (19, 22, and 37 GHz), and the curves are quite similar. The solid lines in the figure show equation (26), and vertical bars show the ± one standard deviation of T_D derived from the radiosondes. For low to moderate values of V (0 to 40 mm), T_D increases with V, and above 40 mm, T_D reaches a relatively constant value of 287 K. The T_U versus V curves (not shown) are very similar except that T_U is 1 to 2 K colder. The following least-square regressions are found to be a good approximation of the T_D, T_U versus V relationship:

$$T_D = b_0 + b_1 V + b_2 V^2 + b_3 V^3 + b_4 V^4 + b_5 (T_S - T_V) \tag{26a}$$

$$T_U = T_D + b_6 + b_7 V \tag{26b}$$

$$T_V = 273.16 + 0.8337\ V - 3.029 \times 10^{-5} V^{3.33} \qquad V \le 48 \tag{27a}$$

$$T_V = 301.16 \qquad V > 48 \tag{27b}$$

where V is in units of millimeters and all temperatures are in units of Kelvin. When evaluating (26a), the expression is linearly extrapolated when V is greater than 58 mm. We have included a small additional term that is a function of the difference between the sea-surface temperature T_S and T_V, which represents the sea-surface temperature that is typical for water vapor V. The term $T_S - T_V$ accounts for the fact that the effective air temperature is typically higher (lower) for the case of unusually warm (cold) water. The T_V versus V relationship was obtained by regressing the climatology sea-surface temperature at the radiosonde site to V derived from the radiosondes. Over the full range of V, the rms error in approximation (26) is typically about 3 K. Table 4 gives the b_0 through b_7 coefficients for all 8 AMSR frequencies.

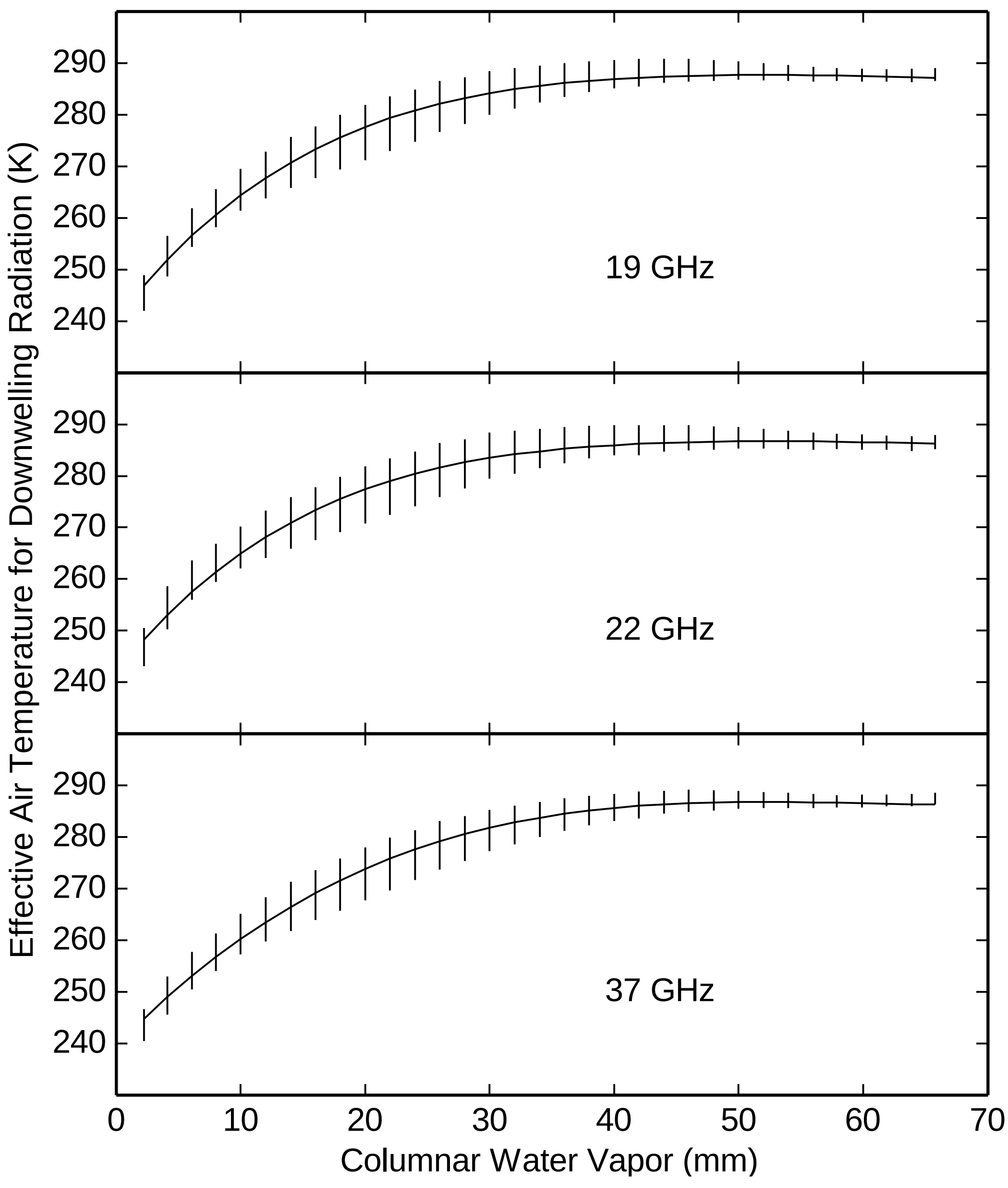

Fig. 4. The effective air temperature T_D for downwelling radiation plotted versus the RAOB columnar water vapor. The solid curve is the model value, and the vertical bars are the ± one standard deviation of T_D derived from radiosondes.

Table 4. Model Coefficients for the Atmosphere

Freq. (GHz)	6.93E+0	10.65E+0	18.70E+0	23.80E+0	36.50E+0	50.30E+0	52.80E+0	89.00E+0
b_0 (K)	239.50E+0	239.51E+0	240.24E+0	241.69E+0	239.45E+0	242.10E+0	245.87E+0	242.58E+0
b_1 (K mm^{-1})	213.92E–2	225.19E–2	298.88E–2	310.32E–2	254.41E–2	229.17E–2	250.61E–2	302.33E–2
b_2 (K mm^{-2})	–460.60E–4	–446.86E–4	–725.93E–4	–814.29E–4	–512.84E–4	–508.05E–4	–627.89E–4	–749.76E–4
b_3 (K mm^{-3})	457.11E–6	391.82E–6	814.50E–6	998.93E–6	452.02E–6	536.90E–6	759.62E–6	880.66E–6
b_4 (K mm^{-4})	–16.84E–7	–12.20E–7	–36.07E–7	–48.37E–7	–14.36E–7	–22.07E–7	–36.06E–7	–40.88E–7
b_5	0.50E+0	0.54E+0	0.61E+0	0.20E+0	0.58E+0	0.52E+0	0.53E+0	0.62E+0
b_6 (K)	–0.11E+0	–0.12E+0	–0.16E+0	–0.20E+0	–0.57E+0	–4.59E+0	–12.52E+0	–0.57E+0
b_7 (K mm^{-1})	–0.21E–2	–0.34E–2	–1.69E–2	–5.21E–2	–2.38E–2	–8.78E–2	–23.26E–2	–8.07E–2
a_{O1}	8.34E–3	9.08E–3	12.15E–3	15.75E–3	40.06E–3	353.72E–3	1131.76E–3	53.35E–3
a_{O2} (K^{-1})	–0.48E–4	–0.47E–4	–0.61E–4	–0.87E–4	–2.00E–4	–13.79E–4	–2.26E–4	–1.18E–4
a_{V1} (mm^{-1})	0.07E–3	0.18E–3	1.73E–3	5.14E–3	1.88E–3	2.91E–3	3.17E–3	8.78E–3
a_{V2} (mm^{-2})	0.00E–5	0.00E–5	–0.05E–5	0.19E–5	0.09E–5	0.24E–5	0.27E–5	0.80E–5

Table 5. RMS Error in Oxygen and Water Vapor Absorption Approximation

Freq. (GHz)	6.93	10.65	18.70	23.80	36.50	50.30	52.80	89.00
Oxygen, A_O	0.0002	0.0002	0.0003	0.0003	0.0008	0.0062	0.0163	0.0009
Vapor, A_V	0.0001	0.0002	0.0011	0.0013	0.0025	0.0042	0.0046	0.0129

The vertically integrated oxygen absorption A_O is nearly constant over the globe, with a small dependence on the air temperature. We find the following expression to be a very good approximation for A_O:

$$A_O = a_{O1} + a_{O2}\left(T_D - 270\right) \tag{28}$$

Table 4 gives the a_O coefficients for the 8 AMSR frequencies, and Table 5 gives the rms error in this approximation for the 8 frequencies. At 23.8 GHz and below, the error is negligible, being 0.0003 napers or less. At 36.5 GHz, the error is still quite small, being 0.0008 napers. Note that 0.001 napers roughly corresponds to a T_B error of 0.5 K. For the 50.3 and 52.8 GHz oxygen band channels, the error is considerably larger, but (28) is not used for the oxygen band channels. Rather the oxygen band channels can be used to retrieve T_D.

The vapor absorption A_V is primarily a linear function of V, although there is a small second order term. We find the following expression is a good approximation for A_V:

$$A_V = a_{V1}V + a_{V2}V^2 \tag{29}$$

Table 4 gives the a_V coefficients for the 8 AMSR frequencies, and Table 5 gives the rms error in this approximation for the 8 frequencies. For the 6.9 and 10.7 AMSR channels, the rms error in this approximation is negligible, being 0.0002 napers or less. In the 18.7 to 36.5 range, the error remains relatively small (0.001 to 0.0025 napers), but not negligible.

The final atmospheric parameter to be specified is the vertically integrated liquid water absorption A_L. When the liquid water drop radius is small relative to the radiation wavelength, the absorption coefficient α_L (cm^{-1}) is given by the Rayleigh scattering approximation [*Goldstein*, 1951]:

$$\alpha_L = \frac{6\pi\rho_L(h)}{\lambda\rho_o} \operatorname{Im}\left(\frac{1-\varepsilon}{2+\varepsilon}\right) \tag{30}$$

where λ is the radiation wavelength (cm), $\rho_L(h)$ is the density (g/cm^3) of cloud water in the atmosphere given as a function of h, ρ_o is the density of water ($\rho_o \approx 1$ g/cm^3), and ε is the complex dielectric constant of water. Note that the dielectric constant varies with temperature and hence is also a function of h. Substituting (30) into (21) gives

$$A_L = \frac{0.6\pi L}{\lambda} \operatorname{Im}\left(\frac{1-\varepsilon}{2+\varepsilon}\right) \tag{31}$$

where L is the vertically integrated liquid water (mm) given by

$$L = 10 \int_0^H dh\ \rho_L(h) \tag{32}$$

The leading factor of 10 converts from g/cm^2 to mm. In deriving (31), we have assumed the cloud is at a constant temperature. For the more realistic case of the temperature varying with height, ε should be evaluated at some mean effective temperature for the cloud. The specification of ε as a function of temperature and frequency is given in Section 2.4. An excellent approximation for (31) is found to be

$$A_L = a_{L1}\left[1 - a_{L2}(T_L - 283)\right] L \tag{33}$$

where T_L is the mean temperature of the cloud, and the a_L coefficients are given in Table 6 for the 8 AMSR frequencies. The error in this approximation is $\leq 1\%$ over the range of T_L from 273 to 288 K, which is negligible compared to other errors such as the uncertainty in specifying the cloud temperature T_L. Note that in the retrieval algorithm, the error in specifying T_L only effects the retrieved value of L. The retrieval of the other parameters only requires the spectral ratio of A_L, which is essentially independent of T_L due to the fact that a_{L2} is spectrally flat.

In the absence of rain, the cloud droplets are much smaller than the radiation wavelengths being considered, and equations (31) and (33) are valid. When rain is present, Mie scattering theory must be used to compute A_L. For light rain not exceeding 2 mm/h and for frequencies between 6 and 37 GHz, the Mie scattering computations give the following approximation:

Table 6. Coefficients for Rayleigh Absorption

Freq (GHz)	6.93	10.65	18.70	23.80	36.50	50.30	52.80	89.00
a_{L1}	0.0078	0.0183	0.0556	0.0891	0.2027	0.3682	0.4021	0.9693
a_{L2}	0.0303	0.0298	0.0288	0.0281	0.0261	0.0236	0.0231	0.0146

$$A_L = a_{L1} L [1 + 3.6 L^{0.3}] \tag{34}$$

In deriving (34) we use a *Marshall and Palmer* [1948] drop size distribution, and L (mm) is now the vertically integrated rain water. This equation is the same as (33) except for the additional $L^{0.3}$ term and the absence of the T_L term. The $L^{0.3}$ term accounts for the fact that the larger water drops are more effective absorbers for a given value of ρ_L. For light rain, the dependence of A_L on temperature is negligible. Comparing (33) and (34) we see that the spectral signature of A_L for light rain is essentially the same as that for non-raining clouds. This invariance in spectral signature of A_L suggests that the retrieval algorithm can be extended to process light rain observations.

2.4. Dielectric Constant of Sea-Water and the Specular Sea Surface

A key component of the sea-surface model is the dielectric constant ε of sea water. The parameter is a complex number that depends on frequency ν, water temperature T_S, and water salinity s. The dielectric constant is given by [*Debye*,1929; *Cole and Cole*, 1941] as

$$\varepsilon = \varepsilon_\infty + \frac{\varepsilon_S - \varepsilon_\infty}{1 + [j\lambda_R/\lambda]^{1-\eta}} - \frac{2j\sigma\lambda}{c} \tag{35}$$

where $j = \sqrt{-1}$, λ (cm) is the radiation wavelength, ε_∞ is the dielectric constant at infinite frequency, ε_S is the dielectric constant for zero frequency (i.e., the static dielectric constant), and λ_R (cm) is the relaxation wavelength. The spread factor η is an empirical parameter that describes the distribution of relaxation wavelengths. The last term accounts for the conductivity of salt water. In this term, σ (sec^{-1}, Gaussian units) is the ionic conductivity and c is the speed of light.

Several investigators have developed models for the dielectric constant of sea water. In the *Stogryn* [1971] model the salinity dependence of ε_S and λ_R was based on the *Lane and Saxton* [1952] laboratory measurements of saline solutions. Stogryn noted that the Lane-Saxton measurements for distilled water did not agree with those of other investigators. The *Klein and Swift* [1977] model is very similar to Stogryn model except that the salinity dependence of ε_S was based on more recent 1.4 GHz measurements [*Ho and Hall*, 1973; *Ho et al.*, 1974]. Klein-Swift noted that their ε_S was significantly different from that derived from the Lane and Saxton measurements. It appears that there may be a problem with Lane-Saxton measurements. However, in the Klein-Swift model, the salinity dependence of λ_R was still based on the Lane-Saxton measurements. We analyzed all the measurements used by Stogryn and Klein-Swift and concluded that the Lane-Saxton measurements of ε for both distilled water and salt water were inconsistent with the results reported by all other investigators. Therefore, we completely exclude the Lane-Saxton measurements from our model derivation.

The model to be presented is very similar to the Klein-Swift model, with two exceptions. First, since we excluded Lane-Saxton measurements, the salinity dependence of λ_R is different. For cold water (0 to 10 C), our λ_R is about 5% lower than the Klein-Swift value and for warm water (30 C), it is about 1% higher. Second, our value for ε_∞ is 4.44 and the Klein-Swift value is 4.9, which was the value used by Stogryn. In the Stogryn model, η = 0, whereas in the Klein-Swift model, $\eta = 0.02$. *Grant et al.* [1957] pointed out that the choice of ε_∞ depends on the choice for η, where $\eta = 0 \rightarrow \varepsilon_\infty = 4.9$ and $\eta = 0.02 \rightarrow \varepsilon_\infty = 4.5$. Thus the Klein-Swift value of $\varepsilon_\infty = 4.9$ is probably too high. In terms of brightness temperatures, these λ_R and ε_∞ differences are most significant at the higher frequencies. For example, at 37 GHz and $\theta_i = 55°$, the difference in specular brightness temperatures produced by our model and the Klein-Swift model differ by about ± 2 K. Analyses of SSM/I observations show that our new model, as compared to the Klein-Swift model, produces more consistent retrievals of ocean parameters. For example, using the Klein-Swift model resulted in an abundance of negative cloud water retrievals in cold water. This problem no longer occurs with the new model. (The negative cloud water problem was the original motivation for doing this reanalysis of the ε model.)

We first describe the dielectric constant model for distilled water, and then extend the model to the more general case of a saline solution. The static dielectric constant ε_{S0} for distilled water has been measured by many investigators. The more recent measurements [*Malmberg and Maryott*, 1956; *Archer and Wang*, 1990] are in very good agreement (0.2%). The *Archer and Wang* [1990] values for ε_{S0}, which are reported in the *Handbook of Chemistry and Physics* [*Lide*,1993], are regressed to the following expression:

$$\varepsilon_{S0} = 87.90 \exp(-0.004585\ t_S) \tag{36}$$

where t_S is the water temperature in Celsius units. The accuracy of the regression relative to the point values for ε_{S0} is 0.01% over the range from 0 to 40 C.

The other three parameters for the dielectric constant of distilled water are the relaxation wavelength λ_{R0}, the spread factor η, and ε_∞. We determine these parameters by a least-squares fit of (35) to laboratory measurements ε_{mea} of the dielectric constant for the range from 1 to 40 GHz. A literature search yielded ten papers reporting ε_{mea} for distilled water. Values for λ_{R0}, η, and ε_∞ are found so as to minimize the following quantity:

$$Q = \left[\mathrm{Re}(\varepsilon - \varepsilon_{mea})\right]^2 + \left[\mathrm{Im}(\varepsilon - \varepsilon_{mea})\right]^2 \tag{37}$$

The relaxation wavelength is a function of temperature [*Grant et al.*, 1957], but it is generally assumed that η and ε_∞ are independent of temperature. The least squares fit yields $\eta = 0.012$, $\varepsilon_\infty = 4.44$, and

$$\lambda_{R0} = 3.30\ \exp(-0.0346\ t_S + 0.00017\ t_S^2) \tag{38}$$

These values are in good agreement with those obtained by other investigators. Our λ_{R0} agrees with the expression derived by *Stogryn* [1971] to within 1%. The values for η (ε_∞) reported in the literature vary from 0 to 0.02 (4 to 5). Note that using a larger value for η necessitates using a smaller value for ε_∞.

The presence of salt in the water produces ionic conductivity σ and modifies ε_S and λ_R. It is generally assumed that η and ε_∞ are not affected by salinity. *Weyl* [1964] found the following regression for the conductivity of sea water.

$$\sigma = 3.39 \times 10^9 C^{0.892} \exp[-\Delta_t \zeta] \tag{39}$$

$$\zeta = 2.03\times10^{-2} + 1.27\times10^{-4}\Delta_t + 2.46\times10^{-6}\Delta_t^2 - C\left(3.34\times10^{-5} - 4.60\times10^{-7}\Delta_t + 4.60\times10^{-8}\Delta_t^2\right) \quad (40)$$

$$C = 0.5536\ s \quad (41)$$

$$\Delta_t = 25 - t_S \quad (42)$$

where s and C are salinity and chlorinity in units of parts/thousand. Note that we have converted the Weyl conductivity to Gaussian units of sec^{-1}.

To determine the effect of salinity on ε_S, we use low frequency (1.43 and 2.65 GHz) measurements of ε for sea water and saline solutions [*Ho and Hall*, 1973; *Ho et al.*, 1974]. For the Ho-Hall data, only the real part of the dielectric constant is used in the fit. Klein and Swift reported that the measurements of the imaginary part were in error. To determine the effect of salinity on λ_R, we use higher frequency (3 to 24 GHz) measurements of ε for saline solutions [*Haggis et al.*, 1952; *Hasted and Sabeh*, 1953; *Hasted and Roderick*, 1958]. A least-squares fit to these data shows that the salinity dependence of ε_S and λ_R can be modeled as

$$\varepsilon_S = \varepsilon_{S0}\ \exp\left(-3.45\times10^{-3}s + 4.69\times10^{-6}s^2 + 1.36\times10^{-5}st_S\right) \quad (43)$$

$$\lambda_R = \lambda_{R0} - 6.54\times10^{-3}\left(1 - 3.06\times10^{-2}t_S + 2.0\times10^{-4}t_S^2\right)s \quad (44)$$

The accuracy of the dielectric constant model is characterized in terms of its corresponding specular brightness temperature T_B. For each laboratory measurement of ε, we compute the specular T_B for an incidence angle of 55° using the Fresnel equation (45) below. Two T_B's are computed: one using ε_{mea} and the other using the model ε coming from the above equations. For the low frequency Ho-Hall data, the rms difference between the 'measurement' T_B and the 'model' T_B is about 0.1 K for v-pol and 0.2 K for h-pol. For the higher frequency data set, the rms difference is 0.8 K for v-pol and 0.5 K for h-pol.

Once the dielectric constant is known, the v-pol and h-pol reflectivity coefficients ρ_V and ρ_H for a specular (i.e., perfectly flat) sea surface are calculated from the well-known Fresnel equations

$$\rho_v = \frac{\varepsilon\cos\theta_i - \sqrt{\varepsilon - \sin^2\theta_i}}{\varepsilon\cos\theta_i + \sqrt{\varepsilon - \sin^2\theta_i}} \quad (45a)$$

$$\rho_h = \frac{\cos\theta_i - \sqrt{\varepsilon - \sin^2\theta_i}}{\cos\theta_i + \sqrt{\varepsilon - \sin^2\theta_i}} \quad (45b)$$

where θ_I is the incidence angle. The power reflectivity R is then given by

$$R_{0p} = \left|\rho_p\right|^2 \quad (46)$$

where subscript 0 denotes that this is the specular reflectivity and subscript p denotes polarization.

2.5. The Wind-Roughened Sea Surface

It is well known that the microwave emission from the ocean depends on surface roughness. A calm sea surface is characterized by a highly polarized emission. When the surface becomes rough, the emission increases and becomes less polarized (except at incidence angles above 55º for which the vertically polarized emission decreases). There are three mechanisms that are responsible for this variation in the emissivity. First, surface waves with wavelengths that are long compared to the radiation wavelength mix the horizontal and vertical polarization states and change the local incidence angle. This phenomenon can be modeled as a collection of tilted facets, each acting as an independent specular surface [*Stogryn,* 1967]. The second mechanism is sea foam. This mixture of air and water increases the emissivity for both polarizations. Sea foam models have been developed by *Stogryn* [1972] and *Smith* [1988]. The third roughness effect is the diffraction of microwaves by surface waves that are small compared to the radiation wavelength. *Rice* [1951] provided the basic formulation for computing the scattering from a slightly rough surface. *Wu and Fung* [1972] and *Wentz* [1975] applied this scattering formulation to the problem of computing the emissivity of a wind-roughened sea surface.

These three effects can be parameterized in terms of the rms slope of the large-scale roughness, the fractional foam coverage, and the rms height of the small-scale waves. Each of these parameters depends on wind speed. *Cox and Munk* [1954], *Monahan and O'Muircheartaigh* [1980], and *Mitsuyasu and Honda* [1982] derived wind speed relationships for the three parameters, respectively. These wind speed relationships in conjunction with the tilt+foam+diffraction model provide the means to compute the sea-surface emissivity. Computations of this type have been done by *Wentz* [1975, 1983] and are in general agreement with microwave observations.

In addition to depending on wind speed, the large-scale rms slope and the small-scale rms height depend on wind direction. The probability density function of the sea-surface slope is skewed in the alongwind axis and has a larger alongwind variance than crosswind variance [*Cox and Munk*, 1954]. The rms height of capillary waves is very anisotropic [*Mitsuyasu and Honda*, 1982]. The capillary waves traveling in the alongwind direction have a greater amplitude than those traveling in the crosswind direction. Another type of directional dependence occurs because the foam and capillary waves are not uniformly distributed over the underlying structure of large-scale waves. *Smith's* [1988] aircraft radiometer measurements show that the forward plunging side of a breaking wave exhibits distinctly warmer microwave emissions than does the back side. In addition, the capillary waves tend to cluster on the downwind side of the larger gravity waves [*Cox,* 1958; *Keller and Wright,* 1975]. The dependence of foam and capillary waves on the underlying structure produces an upwind-downwind asymmetry in the sea-surface emissivity.

The anisotropy of capillary waves is responsible for the observed dependence of radar backscattering on wind direction [*Jones et al.*, 1977]. The upwind radar return is considerably higher than the crosswind return. Also, the modulation of the capillary waves by the underlying gravity waves causes the upwind return to be generally higher than the downwind return. These directional characteristics of the radar return have provided the means to sense wind direction from aircraft and satellite scatterometers [*Jones et al.*, 1979].

To model the rough sea surface, we begin by assuming the surface can be partitioned into foam-free areas and foam-covered areas within the radiometer footprint. The fraction of the total area that is covered by foam is denoted by f. The composite reflectivity is then given by

$$R = (1 - f)R_{clear} + f\kappa R_{clear} \tag{47}$$

where R_{clear} is the reflectivity of the rough sea surface clear of foam, and the factor κ accounts for the way in which foam modifies the reflectivity. As discussed above, foam tends to decrease the reflectivity, and hence $\kappa < 1$. The reflectivity of the clear, rough sea surface is modeled by the following equation:

$$R_{clear} = (1 - \beta)\ R_{geo} \tag{48}$$

where R_{geo} is the reflectivity given by the standard geometric optics model (see below) and the factor $1 - \beta$ accounts for the way in which diffraction modifies the geometric-optics reflectivity. *Wentz* [1975] showed that the inclusion of diffraction effects is a relatively small effect and hence β small compared to unity.

Combining the above two equations gives

$$R = (1 - F)R_{geo} \tag{49}$$

$$F = f + \beta - f\beta - f\kappa + f\kappa\beta \tag{50}$$

where F is a 'catch-all' term that accounts for both foam and diffraction effects. All of the terms that makeup F are small compared to unity, and the results to be presented show that F < 10%. The reason we lump foam and diffraction effects together is that they both are difficult to model theoretically. Hence, rather than trying to compute F theoretically, we let F be a model parameter that is derived empirically from various radiometer experiments. However, the R_{geo} term is theoretically computed from the geometric optics. Thus, the F term is a measure of that portion of the wind-induced reflectivity that is not explained by the geometric optics.

The geometric optics model assumes the surface is represented by a collection of tilted facets, each acting as an independent reflector. The distribution of facets is statistically characterized in terms of the probability density function $P(S_u,S_c)$ for the slope of the facets, where S_u and S_c are the upwind and crosswind slopes respectively. Given this model, the reflectivity can be computed from equation (7). To do this, the integration variables θ_s,ϕ_s in (7) are transformed to the surface slope variables. The two equations governing this transformation are

$$\mathbf{k}_s = \mathbf{k}_i - 2(\mathbf{k}_i \cdot \mathbf{n})\mathbf{n} \tag{51}$$

$$\mathbf{n} = \frac{[-S_u,\ -S_c,\ 1]}{\sqrt{1 + S_u^2 + S_c^2}} \tag{52}$$

where **n** is the unit normal vector for a given facet. Transforming (7) to the S_u,S_c integration variables yields

$$R_{geo} = \frac{\int dS_u \int dS_c P(S_u,S_c)\sqrt{1+S_u^2+S_c^2}\,(\mathbf{k_i}\cdot\mathbf{n})\left|(\mathbf{p}\cdot\mathbf{h_i})\rho_h\mathbf{h_s} + (\mathbf{p}\cdot\mathbf{v_i})\rho_v\mathbf{v_s}\right|^2[\chi(\mathbf{k_s})(1-R_\times)+R_\times]}{\int dS_u \int dS_c P(S_u,S_c)\sqrt{1+S_u^2+S_c^2}\,(\mathbf{k_i}\cdot\mathbf{n})} \quad (53)$$

where $\mathbf{p}$ is the unit vector specifying the reflectivity polarization. The unit vectors $\mathbf{h_i}$ and $\mathbf{v_i}$ ($\mathbf{h_s}$ and $\mathbf{v_s}$) are the horizontal and vertical polarization vectors associated with the propagation vector $\mathbf{k_i}$ ($\mathbf{k_s}$) as measured in the tilted facet reference frame. These polarization vectors in the tilted frame of reference are given by

$$\mathbf{h_j} = \frac{\mathbf{k_j}\times\mathbf{n}}{|\mathbf{k_j}\times\mathbf{n}|} \quad (54a)$$

$$\mathbf{v_j} = \mathbf{k_j}\times\mathbf{h_j} \quad (54b)$$

where subscript j = i or s. The terms ρ_v and ρ_h are the v-pol and h-pol Fresnel reflection coefficients given above. The last factor in (53) accounts for multiple reflection (i.e., radiation reflecting off of one facet and then intersecting another). $\chi(\mathbf{k_s})$ is the shadowing function given by *Wentz* [1975], and $R_\times$ is the reflectivity of the secondary intersection. The shadowing function $\chi(\mathbf{k_s})$ essentially equals unity except when $\mathbf{k_s}$ approaches surface grazing angles.

The interpretation of (53) is straightforward. The integration is over the ensemble of tilted facets having a slope probability of $P(S_u,S_c)$. The term $\sqrt{1+S_u^2+S_c^2}\,(\mathbf{k_i}\cdot\mathbf{n})$ is proportional to the solid angle subtended by the tilted facet as seen from the observation direction specified by $\mathbf{k_i}$. The term $\left|(\mathbf{p}\cdot\mathbf{h_i})\rho_h\mathbf{h_s} + (\mathbf{p}\cdot\mathbf{v_i})\rho_v\mathbf{v_s}\right|^2$ is the reflectivity of the tilted facet. And, the denominator in (53) properly normalizes the integral.

To specify the slope probability we use a Gaussian distribution as suggested by *Cox and Munk* [1954], and we assume that the upwind and crosswind slope variances are the same. Wind direction effects are considered in Section 2.7. Then, the slope probability is given by

$$P(S_u,S_c) = \left(\pi\Delta S^2\right)^{-1}\exp\left(\frac{-S_u^2-S_c^2}{\Delta S^2}\right) \quad (55)$$

where ΔS^2 is the total slope variance defined as the sum of the upwind and crosswind slope variances. Ocean waves with wavelengths shorter than the radiation wavelength do not contribute to the tilting of facets and hence should not be included in the ensemble specified by $P(S_u,S_c)$. For this reason, the effective slope variance ΔS^2 increases with frequency, reaching a maximum value referred to as the optical limit. The results of *Wilheit and Chang* [1980] and *Wentz* [1983] indicate that the optical limit is reached near ν = 37 GHz. Hence, for $\nu \geq$ 37 GHz, we use the *Cox and Munk* [1954] expression for optical slope variance. For lower frequencies, a reduction factor is applied to the Cox and Munk expression. This reduction factor is based on ΔS^2 values derived from the SeaSat SMMR observations [*Wentz*, 1983].

$$\Delta S^2 = 5.22\times10^{-3}W \qquad \nu \geq 37 \text{ GHz} \quad (56a)$$

$$\Delta S^2 = 5.22\times10^{-3}\left[1-0.00748(37-\nu)^{1.3}\right]W \qquad \nu < 37 \text{ GHz} \quad (56b)$$

where W is the wind speed (m/s) measured 10 m above the surface. Note the Cox and Munk wind speed was measured at a 12.5 m elevation. Hence, their coefficient of 5.12×10^{-3} is increased by 2% to account for our wind being referenced to a 10 m elevation.

The sea-surface reflectivity R_{geo} is computed for a range of winds varying from 0 to 20 m/s, for a range of sea-surface temperatures varying from 273 to 303 K, and for a range of incidence angles varying from 49° to 57°. These computations require the numerical evaluation of the integral in equation (53). The integration is done over the range $S_u^2 + S_c^2 \le 4.5\Delta S^2$. Facets with slopes exceeding this range contribute little to the integral, and it is not clear if a Gaussian slope distribution is even applicable for such large slopes. Analysis shows that the computed ensemble of R_{geo} is well approximated by the following regression:

$$R_{geo} = R_0 - \left[r_0 + r_1(\theta_i - 53) + r_2(T_S - 288) + r_3(\theta_i - 53)(T_S - 288)\right]W \qquad (57)$$

where the first term R_0 is the specular power reflectivity given by (46) and the second term is the wind-induced component of the sea-surface reflectivity. The r coefficients are given in Table 7 for all AMSR channels. Equation (57) is valid over the incidence angle from 49° to 57°. It approximates the θ_i and T_S variation of R_{geo} with an equivalent accuracy of 0.1 K. The approximation error in the wind dependence is larger. In the geometric optics computations, the variation of R_{geo} with wind is not exactly linear. In terms of T_B, the non-linear component of R_{geo} is about 0.1 K at the lower frequencies and 0.5 K at the higher frequencies. However, in view of the general uncertainty in the geometric optics model, we will use the simple linear expression for R_{geo}, and let the empirical F term account for any residual non-linear wind variations, as is discussed in the next paragraph.

Table 7. Model Coefficients for Geometric Optics

Freq. (GHz)	6.93E+0	10.65E+0	18.70E+0	23.80E+0	36.50E+0	50.30E+0	52.80E+0	89.00E+0
v-pol r_0	–0.27E–03	–0.32E–03	–0.49E–03	–0.63E–03	–1.01E–03	–1.20E–03	–1.23E–03	–1.53E–03
h-pol r_0	0.54E–03	0.72E–03	1.13E–03	1.39E–03	1.91E–03	1.97E–03	1.97E–03	2.02E–03
v-pol r_1	–0.21E–04	–0.29E–04	–0.53E–04	–0.70E–04	–1.05E–04	–1.12E–04	–1.13E–04	–1.16E–04
h-pol r_1	0.32E–04	0.44E–04	0.70E–04	0.85E–04	1.12E–04	1.18E–04	1.19E–04	1.30E–04
v-pol r_2	0.01E–05	0.11E–05	0.48E–05	0.75E–05	1.27E–05	1.39E–05	1.40E–05	1.15E–05
h-pol r_2	0.00E–05	–0.03E–05	–0.15E–05	–0.23E–05	–0.36E–05	–0.32E–05	–0.30E–05	0.00E–05
v-pol r_3	0.00E–06	0.08E–06	0.31E–06	0.41E–06	0.45E–06	0.35E–06	0.32E–06	–0.09E–06
h-pol r_3	0.00E–06	–0.02E–06	–0.12E–06	–0.20E–06	–0.36E–06	–0.43E–06	–0.44E–06	–0.46E–06
r_0 in units of s/m, r_1 in units of s/m-deg, r_2 in units of s/m-K, r_3 in units of s/m-deg-K								

In the 19-37 GHz band, the F term is found from collocated SSM/I-buoy observations. The procedure for finding F is essentially the same as described by *Wentz* [1997] for finding the wind-induced emissivity, but in this case we first remove the geometric optics contribution to R. The F term is found to be a monotonic function of wind speed described by

$$F = m_1 W \qquad W < W_1 \qquad (58a)$$

$$F = m_1 W + \tfrac{1}{2}(m_2 - m_1)(W - W_1)^2 / (W_2 - W_1) \qquad W_1 \le W \le W_2 \qquad (58b)$$

$$F = m_2 W - \tfrac{1}{2}(m_2 - m_1)(W_2 + W_1) \qquad W > W_2 \qquad (58c)$$

This equation represents two linear segments connected by a quadratic spline such that the function and its first derivative are continuous. The spline points W_1 and W_2 are 7 and 12 m/s, respectively. The m coefficients are found so that the T_B model matches the SSM/I observations when the buoy wind is used to specify W. Over the SSM/I range for frequencies from 19 to 37 GHz, we find that m_1 and m_2 are independent of both frequency and polarization. We find that $m_1 = 0.00254$ s/m and $m_2 = 0.00915$ s/m for $\nu \ge 19$ GHz.

At AMSR's lower frequencies of 6.9 and 10.7 GHz, there is no SSM/I data, and instead we use the collocated SMMR-SASS data set which has scatterometer wind speeds collocated with SMMR T_B's. To support this analysis we also consider the radiometer observations made by *Hollinger* [1971] and *Webster et al.* [1976]. We interpolated the SMMR-SASS and Hollinger and Webster results to the AMSR frequencies of 6.9 and 10.7 GHz. In addition, the SMMR-SASS and Hollinger results are interpolated to the AMSR incidence angle of 55°. However, Webster's results are all at 0° and 38°, and no θ_i interpolation is done (see below). Table 8 gives the change in brightness temperature ΔT_B per change in wind speed ΔW derived from the different investigations. The derivative $\Delta T_B/\Delta W$ (Ks/m) is simply defined as

$$\frac{\Delta T_B}{\Delta W} = 290 \frac{\Delta E}{\Delta W} \qquad (59)$$

where ΔE is the wind-induced change in emissivity and 290 represents a typical sea-surface temperature. Hollinger's observations were made during moderate winds and the effects of sea foam were removed. In contrast, Webster's observations were made during high winds and included sea foam. In view of this, we show two cases in Table 8: moderate wind and high winds. For the moderate wind case, the agreement between $\Delta T_B/\Delta W$ derived from SMMR-SASS and that reported by Hollinger is very good. However, for the high wind case, the agreement is not as good. Webster's $\Delta T_B/\Delta W$ is significantly higher than the value derived form SMMR-SASS. As mentioned above Webster's results are at an incidence angle

Table 8. Change in Brightness Temperature Due to Wind Speed

$\Delta T_B/\Delta W$ (Ks/m), Moderate Wind Case, W= 7 m/s				
	6.9 GHz, v-pol	6.9 GHz, h-pol	10.7 GHz, v-pol	10.7 GHz, h-pol
SMMR-SASS	0.09	0.50	0.11	0.63
Hollinger	0.07	0.52	0.04	0.65
$\Delta T_B/\Delta W$ (Ks/m), High Wind Case, W= 16 m/s				
	6.9 GHz, v-pol	6.9 GHz, h-pol	10.7 GHz, v-pol	10.7 GHz, h-pol
SMMR-SASS	0.32	0.73	0.35	0.92
Webster	0.61	1.09	0.70	1.25

of 38° whereas the SMMR-SASS results have been interpolated to 55°. But this does not explain the discrepancy since one expects the h-pol $\Delta T_B/\Delta W$ to increases with incidence angle. We place more confidence on the satellite data set, and will use the SMMR-SASS analysis to specify the wind-induced emissivity at 6.9 and 10.7 GHz.

Values for m_1 and m_2 are found from the SMMR-SASS data for 6.9 and 10.7 GHz. The value at 6.9 GHz (10.7 GHz) is about 60% (80%) of the value at 19 GHz. It appears that at low frequencies m_1 and m_2 increase rapidly with frequency and then flatten out and reach a maximum when $\nu \approx 19$ GHz. The following expressions model this behavior

$$m_1 = 2.89\times10^{-4}\nu - 9.28\times10^{-6}\nu^2 + 5.83\times10^{-8}\nu^3 \qquad \nu \le 19 \text{ GHz} \qquad (60a)$$

$$m_2 = 8.42\times10^{-4}\nu - 1.26\times10^{-5}\nu^2 - 3.35\times10^{-7}\nu^3 \qquad \nu \le 19 \text{ GHz} \qquad (60b)$$

where ν is frequency (GHz). These expressions monotonically increase with ν up to 19 GHz, at which m_1 = 0.00254 s/m and m_2 = 0.00915 s/m and $\partial m/\partial\nu = 0$. For $\nu > 19$ GHz, m_1 and m_2 are held at their 19-GHz value. As was the case at the SSM/I frequencies, m_1 and m_2 are found to be independent of polarization.

These results indicate that diffraction plays a significant role in modifying the sea-surface reflectivity. If diffraction were not important, β would be 0 in equation (50), and F would be proportional to the fractional foam coverage f. Since f is essentially zero for W < 7 m/s, m_1 would be 0. This is not the case, and we interpret the m_1 coefficient as an indicator of diffraction.

2.6. Atmospheric Radiation Scattered by the Sea Surface

The downwelling atmospheric radiation incident on the rough sea surface is scattered in all directions. The scattering process is governed by the radar cross section coefficients σ_o as indicated by equation (14). For a perfectly flat sea surface, the scattering process reduces to simple specular reflection, for which radiation coming from the zenith angle θ_s is reflected into zenith angle θ_i , where $\theta_s = \theta_i$. In this case, the reflected sky radiation is simply RT_{BD}. However, for a rough sea surface, the tilted surface facets reflect radiation for other parts of the sky into the direction of zenith angle θ_i. Because the downwelling radiation T_{BD} increases as the secant of the zenith angle, the total radiation scattered from the sea surface is greater than that given by simple specular reflection. The sea-surface reflectivity model discussed in the previous section is used to compute the scattered sky radiation $T_{B\Omega}$. These computations show that $T_{B\Omega}$ can be approximated by

$$T_{B\Omega} = [(1+\Omega)(1-\tau)(T_D - T_C) + T_C]\ R \qquad (61)$$

where R is the sea-surface reflectivity given by (49), T_{BD} is the downwelling brightness temperature from zenith angle θ_i given by (24), and Ω is the fit parameter. The second term in the brackets is the isotropic component of the cold space radiation. This constant factor can be removed from the integral. The fit parameter for v-pol and h-pol is found to be

$$\Omega_V = [2.5 + 0.018(37-\nu)\ ][\Delta S^2 - 70.0\Delta S^6]\ \tau^{3.4} \qquad (62a)$$

$$\Omega_H = [6.2 - 0.001(37-\nu)^2][\Delta S^2 - 70.0\Delta S^6]\ \tau^{2.0} \qquad (62b)$$

where ν is frequency (GHz) and ΔS^2 is the effective slope variance given by (56). The term $\Delta S^2 - 70.0\Delta S^6$ reaches a maximum at $\Delta S^2 = 0.069$. For $\Delta S^2 > 0.069$, the term is held at its maximum value of 0.046. Ω_V has a linear dependence on frequency, whereas Ω_H has a quadratic dependence, reaching a maximum value at $\nu = 37$ GHz. For $\nu > 37$ GHz, Ω_H is held constant at this maximum value. Approximation (62) is valid for the range of incidence angles from 52° to 56°. For moderately high winds (12 m/s) and a moist atmosphere (high vapor and/or heavy clouds), the scattering process increases the reflected 37 GHz radiation by about 1 K for v-pol and 5 K for h-pol. At 7 GHz, the increase is much less, being about 0.2 K for v-pol and 0.8 K for h-pol. The accuracy of the above approximation as compared to the theoretical computation is about 0.03 K and 0.2 K at 7 and 37 GHz, respectively. Note that when the atmospheric absorption becomes very large (i.e., τ is small), Ω tends to zero because the sky radiation for a completely opaque atmosphere is isotropic.

2.7. Wind Direction Effects

The anisotropy of the sea-surface roughness produces a variation of the brightness temperature versus wind direction, as discussed in Section 2.5. In the 19 to 37 GHz band, *Wentz* [1992] determined this wind direction signal using collocated SSM/I T_B's and buoy wind vectors. At an incidence angle near 53°, the wind direction signal exhibits the following second-order harmonic variation with wind direction:

$$\Delta E_{19-37} = \gamma_1 \cos\phi + \gamma_2 \cos 2\phi \tag{63}$$

where ΔE is the change in the sea-surface emissivity and ϕ is the wind-direction angle relative to the azimuth-look angle. When $\phi = 0°$ (180°), the observation is upwind (downwind). The subscript 19-37 denotes that the results are for the 19-37 GHz band. The amplitude coefficients γ_1 and γ_2 are found to be essentially the same for both 19 and 37 GHz. The coefficients are different for the two polarizations and do vary with wind speed as given below

$$\gamma_{1V} = 7.83\times10^{-4} W - 2.18\times10^{-5} W^2 \tag{64a}$$

$$\gamma_{2V} = -4.46\times10^{-4} W + 3.00\times10^{-5} W^2 \tag{64b}$$

$$\gamma_{1H} = 1.20\times10^{-3} W - 8.57\times10^{-5} W^2 \tag{64c}$$

$$\gamma_{2H} = -8.93\times10^{-4} W + 3.76\times10^{-5} W^2 \tag{64d}$$

In *Wentz* [1992], the wind direction signal was expressed in terms of a brightness temperature change rather than an emissivity change, and the wind speed was referenced to a 19.5 m anemometer height. In the above equations, we have converted the *Wentz* [1992] expressions from ΔT_B to ΔE and use a 10 m reference height for W.

Little is known about the wind direction signal for frequencies below 19 GHz. Some very preliminary data from the Japanese AMSR aircraft simulations suggests that the signal decreases with decreasing frequency. Other than this, there are no experimental data on the variation of T_B versus ϕ at 6.9 and 10.7 GHz. Thus, we must make an educated guess on what will be observed at these lower frequencies. We know that the wind speed signal decreases rapidly with decreasing frequency below 19 GHz, as is indicated by Table 4 and equation (60). It seems reasonable to assume that the wind direction signal will decrease in the same way as the wind signal decreases. This assumption is expressed by

$$\Delta E = \frac{m_1 \, \Delta E_{19-37}}{0.00254} \qquad \nu < 19 \text{ GHz} \tag{65}$$

where m_1 is the frequency dependent wind speed parameter given by (60a). At ν = 19 GHz, m_1 = 0.00254, and $\Delta E = \Delta E_{19\text{-}37}$. At ν = 6.9 GHz, m_1 = 0.00157, and hence the wind direction signal is 60% of the 19-37 GHz value.

3. The Ocean Retrieval Algorithm

3.1 Introduction

In general, there are three types of ocean retrieval algorithms:

1. Multiple linear regression algorithms
2. Non-linear, iterative algorithms
3. Post-launch *in-situ* regression algorithms

The first two types are physical algorithms in the sense that radiative transfer theory is used in their derivation. The third type is purely statistical with little or no consideration of the underlying physics. We now describe each of these algorithms and discuss their strengths and weaknesses.

3.2 Multiple Linear Regression Algorithm

Consider a linear process in which a set of inputs denoted by the column vector **X** is transformed to a set of outputs denoted by the column vector **Y**. The linear process is then characterized by the matrix **A** that relates **Y** to **X**.

$$\mathbf{Y} = \mathbf{AX} \tag{66}$$

The measurement of Y usually contains some noise **e** and is denoted by

$$\tilde{\mathbf{Y}} = \mathbf{Y} + \varepsilon = \mathbf{AX} + \varepsilon \tag{67}$$

The retrieval problem is then to estimate **X** given $\tilde{\mathbf{Y}}$. The most commonly used criteria for estimating **X** is to find **X** such that the variance between **Y** and $\tilde{\mathbf{Y}}$ is minimized. Using this criteria, one finds the well known least-squares solution:

$$\hat{\mathbf{X}} = (\mathbf{A}^{\mathbf{T}}\Xi^{-1}\mathbf{A})^{-1}\mathbf{A}^{\mathbf{T}}\Xi^{-1}\tilde{\mathbf{Y}} \tag{68}$$

where **X** is the correlation matrix for the error vector **e**. If the errors are uncorrelated, then **X** is diagonal.

For our application, the system input vector **X** is the set of geophysical parameters **P** and the output vector $\tilde{\mathbf{Y}}$ is the set of T_B measurements. Note that X and Y can be non-linear functions of P and T_B, respectively without violating the requirement for linearity between **X** and **Y**. For example, the relationship between T_B and atmospheric parameters V and L can be approximated by

$$T_B \approx T_E\left\{1 - R\ \exp\left[-2\sec\theta_i\left(A_O + a_V V + a_L L\right)\right]\right\} \tag{69}$$

where T_E is an effective temperature of the ocean-atmosphere system which is relatively constant. Then,

$$\ln(T_E - T_B) = \ln(RT_E) - 2\sec\theta_i\left(A_O + a_V V + a_L L\right) \tag{70}$$

From this we see that the relationship between T_B and V, L can be linearized by transforming from **Y** = T_B to **Y** = $\ln(T_E - T_B)$. *Wilheit and Chang* [1980] followed this approach and used a value of 280 K for T_E. As a further extension, **Y** can also include higher order terms such as T_B^2 and $T_{B37V}\,T_{B23H}$.

Likewise, the input X can be a nonlinear transformation of the geophysical parameters P. For example, the wind speed dependence of T_B (i.e., $\partial T_B/\partial W$) increases with wind speed, and the relationship can be made more linear by the following transformation

$$W' = W \qquad W < W_1 \tag{71a}$$

$$W' = W + M_1(W - W_1)^2 \qquad W_1 \le W \le W_2 \tag{71b}$$

$$W' = M_2 W - M_3 \qquad W > W_2 \tag{71c}$$

This transformation represents two linear segments connected by a quadratic spline such that the function and its first derivative are continuous.

Thus the requirement of linearity is not as constraining as it might first appear, and a generalized linear statistical regression algorithm can be represented by

$$P_j = \Re\left[c_{0j} + \sum_{i=1}^{I} c_{ij}\Im(T_{Bi})\right] \tag{72}$$

where $\Im$ and $\Re$ are linearizing functions. Subscript i denotes the AMSR channel (1 = 6.9V, 2 = 6.9H, etc.), and subscript j denotes the parameter to be retrieved (1 = T_S, 2 = W, 3 = V, 4 = L). For AMSR, our initial design for the linear regression algorithm discussed in the next section uses the following linearizing functions:

$$\Im(T_B) = T_B \qquad \nu = 6.9 \text{ and } 10.7 \text{ GHz} \tag{73a}$$

$$\Im(T_B) = -\ln(290 - T_B) \qquad \nu = 18.7, 23.8, \text{ and } 36.5 \text{ GHz} \tag{73b}$$

$$\Re(X) = X \tag{74}$$

After testing the initial algorithm, we will experiment with additional linearizing functions, such as the wind speed linearization given by (71).

In principle, the c_{ij} coefficients can be found from (68) given the **A** matrix and the error correlation matrix **X**. However, even after the linearizing functions are applied, the relationship of **Y** versus **X** is not strictly linear, and the elements of **A** matrix are not constant, but rather vary with **P**. One could find a linear approximation for the **Y** versus **X** relationship, and then derive the c_{ij} coefficients from (68). However, we prefer the more direct approach suggested by *Wilheit and Chang* [1980] in which brightness temperatures are computed for an ensemble of environmental scenes and then multiple linear regression is used to derive the c_{ij} coefficients, as is discussed in the following section.

3.3. Derivation and Testing of the Linear Regression Algorithm

The derivation of the c_{ij} coefficients in the AMSR linear regression algorithm is shown in Figure 5. A large ensemble of ocean-atmosphere scenes are first assembled. The specification of the atmospheres comes from 42,195 quality-controlled radiosonde flights launched

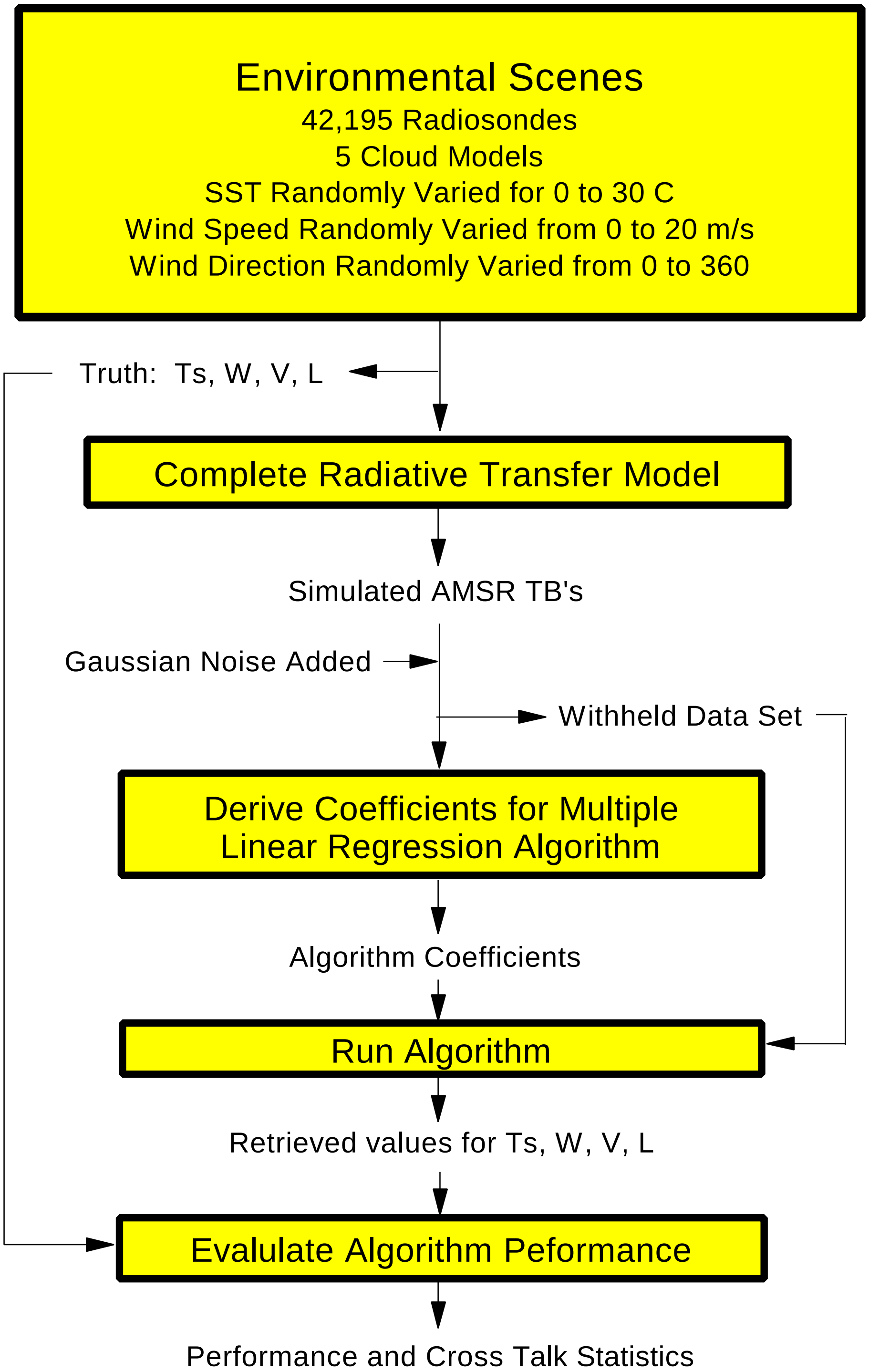

Fig. 5. Derivation and testing of the linear regression algorithm

from small islands during the 1987 to 1990 time period [*Wentz*, 1997]. One half of these radiosonde flights are used for deriving the c_{ij} coefficients, and the other half is withheld for testing the algorithm. A cloud layer of various columnar water densities ranging from 0 to 0.3 mm is superimposed on the radiosonde profiles. Underneath these simulated atmospheres, we place a rough ocean surface. The sea-surface temperature T_S is randomly varied from 0 to 30 C, the wind speed W is randomly varied from 0 to 20 m/s, and the wind direction ϕ is randomly varied from 0 to 360°. About 400,000 scenes are generated in this manner.

In nature, there is a strong correlation between T_S and W. We could have incorporated this correlation into the ensemble of the scene. For example, we could have discarded cases of very cold water and very high water vapor, which never occur in nature. However, for now we include these unrealistic cases in order to determine if the algorithm is truly capable of separating the T_S signal from the V signal.

Atmospheric brightness temperatures T_{BU} and T_{BD} and transmittance τ are computed from the radiosonde + cloud profiles of T(h), p(h), ρ_V(h), and ρ_L(h) using equations (17), (18) and (19). The reflectivity R of the rough sea surface is computed according to the equations given in Section 2.5, and the atmospheric radiation scattered from the sea surface $T_{B\Omega}$ is computed from (61). Wind direction effects are included as described in Section 2.7. Finally, the brightness temperature T_B as seen by AMSR is found by combining the atmospheric and sea-surface components, as is expressed by (10).

Noise is added to the simulated AMSR T_B's. This noise represents the measurement error in the AMSR T_B's. The measurement error depends on the spatial resolution. At a 60-km resolution, which is commensurate with the 6.9 GHz footprint, the measurement error is 0.1 K. A random number generator is used to produce Gaussian noise having a standard deviation of 0.1 K. This noise is added to the simulated T_B's. At this point in the simulation, we could also add modeling error to the T_B's. Modeling error accounts for the difference between the model and nature. It is a very difficult parameter to determine since it involves physical processes which are not sufficiently understood to be included in the current model. For now, we are not including any modeling error in the simulations, but we will be investigating this problem in the future.

Given the noise-added simulated T_B's, the standard multiple linear regression technique is used to find the c_{ij} coefficients. The coefficients are found such that the rms difference between P_j and the true value for the specified environmental scene is minimized. For the initial set of simulations, we use all 10 lower frequency channels (i.e., 6.9, 10.7, 18.7, 23.8 and 36.5 GHz, dual polarization). Later on, we will investigate the utility of using a reduced set of channels.

The algorithm is tested by repeating the above process, only this time using the withheld environmental scenes. The geophysical parameters T_S, W, V, and L are computed from the noise-added T_B's using equation (72). Statistics on the error in P_i are accumulated. The results are shown in Figure 6. The solid line in the figure shows the mean retrieval error, and the dashed lines show the one standard deviation envelope. The retrieval error for each of the four parameters is plotted versus the four parameters in order to show the crosstalk error

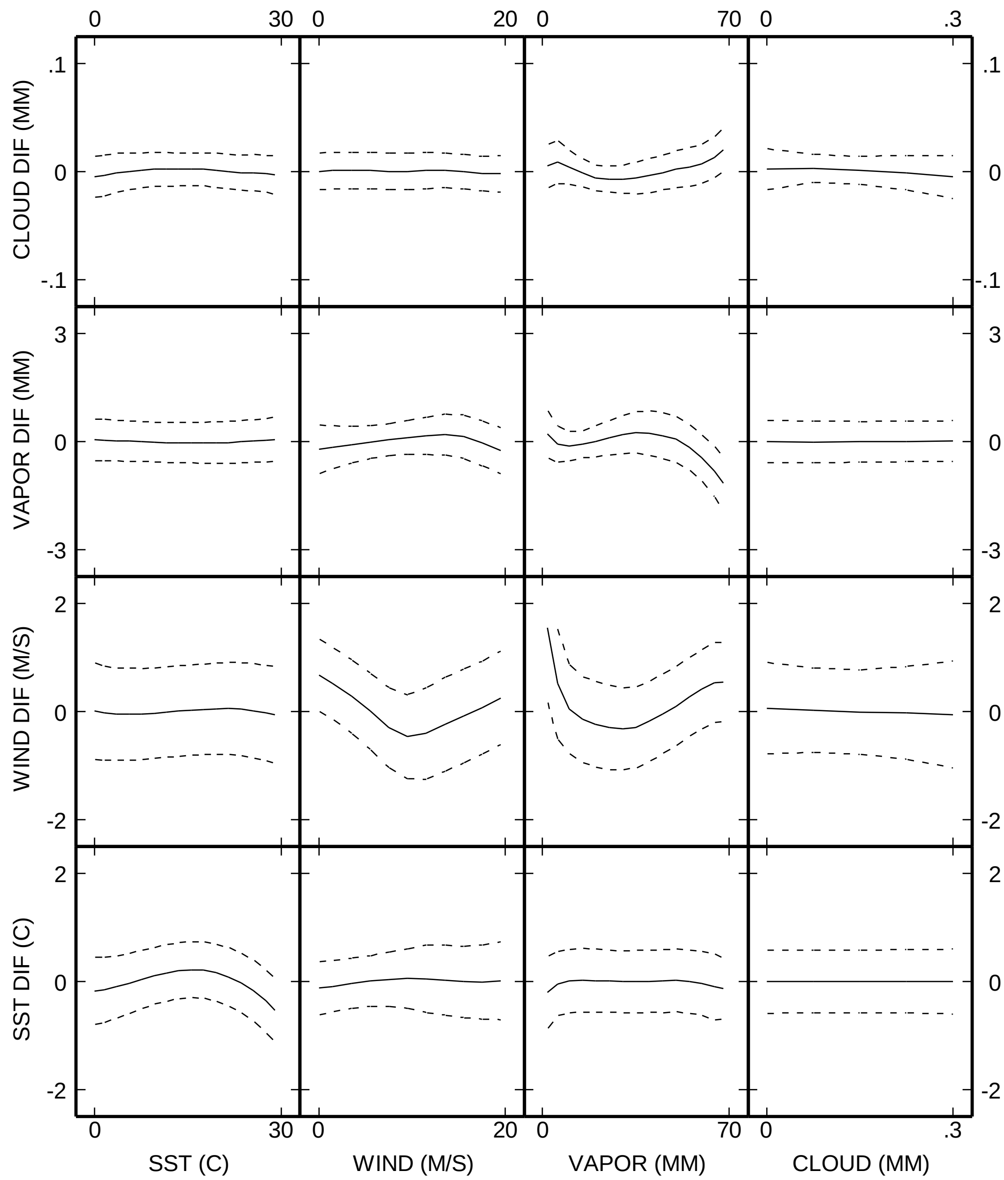

Fig 6. Preliminary results for the linear statistical regression algorithm for AMSR. The solid line in the figure shows the mean retrieval error, and the dashed lines show the one standard deviation envelope. The retrieval error for each of the four parameters is plotted versus the four parameters in order to show the crosstalk error matrix. The diagonal in the crosstalk matrix verifies that the dynamic range of a given parameter is correct, and the off-diagonal plots verifies that there is no crosstalk error in the retrieval.

matrix. The diagonal in the crosstalk matrix verifies that the dynamic range of a given parameter is correct, and the off-diagonal plots verify that there is no crosstalk error in the retrieval.

The results look quite good. There is a little crosstalk, but it is quite small. Table 9 gives the overall rms error for the retrievals. Wind direction variability is a major source of error in the T_S retrieval. When wind direction variability is removed from the simulations, the T_S retrieval error decreases to 0.3 C. The wind direction problem is further discussed in Sections 1.5 and 4.3.

We again emphasize that these results are very preliminary. There is much more work to do. For example, the cloud models need to be more variable and the performance of the relatively simple LSR algorithm needs to be compared with the non-linear algorithm discussed in the next section.

Table 9. Preliminary Estimate of Retrieval Error

Ocean Parameter	Rms Error
Sea-Surface Temperature	0.58 C
Wind Speed	0.86 m/s
Columnar Water Vapor	0.57 mm
Columnar Cloud Water	0.017 mm

3.4. Non-Linear, Iterative Algorithm

The major shortcoming of the multiple linear regression algorithm is that the non-linearities in the T_B versus **P** relationship are handled in an *ad hoc* manner. The linearization functions are only approximations, and the inclusion of second order terms such as T_B^2 and T_{B37V} T_{B23H} do not really describe the inverse of the T_B versus **P** relationship. A more rigorous treatment of the non-linearity problem is to express the T_B versus **P** relationship in terms of a non-linear model function F(**P**), and then invert the following set of equations

$$T_{Bi} = F_i(\mathbf{P}) + \varepsilon_i \tag{75}$$

where subscript i denotes the observation number and ε_i is the measurement noise. The number of observations must be equal to or greater than the number of unknown parameters (i.e., the number of elements in **P)**. For each set of AMSR observations, equations (75) are inverted to yield **P**. This method is much more numerically intensive than the linear regression algorithm in which there is a fixed relationship between **P** and T_B. However, given today's computers, the computational burden is no longer a problem.

Equation (75) is solved using an extension of Newton's iterative method. In Newton's method, the model function is expressed as a Taylor expansion:

$$T_{Bi} = F_i(\overline{\mathbf{P}}) + \sum_{j=1}^{4} \left(P_j - \overline{P}_j\right) \left.\frac{\partial F_i}{\partial P_j}\right|_{\overline{\mathbf{P}}} + O^2 + \varepsilon_i \tag{76}$$

where $\overline{\mathbf{P}}$ is a first guess value for **P** and O^2 represents the higher order terms in the expansion. This system of simultaneous equations is written in matrix form as

$$\Delta\mathbf{T_B} = \mathrm{A}\ \Delta\mathbf{P} + \mathbf{O^2} + \varepsilon \tag{77}$$

where **A** is a matrix of $i \times j$ elements and $\mathbf{DT_B}$, **DP**, and **e** are column vectors. The elements of **A,** $\mathbf{DT_B}$, and **DP** are

$$A_{ij} = \left.\frac{\partial F_i}{\partial P_j}\right|_{\overline{\mathbf{P}}} \tag{78}$$

$$\Delta T_{Bi} = T_{Bi} - F_i(\overline{\mathbf{P}}) \tag{79}$$

$$\Delta P_j = P_j - \overline{P}_j \tag{80}$$

Equation (77) is solved by ignoring the higher order terms (i.e., by setting O^2 to zero), and the solution is

$$\mathbf{P} = \overline{\mathbf{P}} + (\mathbf{A^T}\Xi^{-1}\mathbf{A})^{-1}\mathbf{A^T}\Xi^{-1}\Delta\mathbf{T_B} \tag{81}$$

where **X** is the error correlation matrix. This procedure is then repeated with **P** from (81) replacing $\overline{\mathbf{P}}$, and several such iterations are performed. For the no-noise case (**e** = 0), **X** drops out of the formulation and an exact solution is obtained when $\mathbf{DT_B}$ goes to zero. For the noise case, a solution is found when $\mathbf{DT_B}$ reaches some constant minimum value.

The solution of P can be constrained by the inclusion of *a priori* information. This is accomplished by including additional equations in (77). For example, if ancillary information on wind direction were available, then the following equation could be added to (77)

$$\phi = \hat{\phi} + \varepsilon_\phi \tag{82}$$

where $\hat{\phi}$ is the a priori estimate of ϕ and ε_ϕ is the rms uncertainty in that estimate. Similar constraining equations can be included for other types of information such as the vertical distribution of water vapor and air temperature.

In general, there is no guarantee that a solution will be found using this method. Furthermore, if a solution is found, there is no guarantee that it is an unique solution. However for the case of AMSR, the relationships between **P** and T_B are quasi-linear in that $\partial T_B/\partial P > 0$ for all channels except 36.5 GHz in cold water, for which $\partial T_B/\partial T_S$ is < 0. Experience has shown that a solution is nearly always found. It also appears that this solution is unique, but this needs to be verified.

We have been assuming that the T_B versus **P** relationship can be exactly described by a non-linear model function F. In this case, the non-linear, iterative algorithm has the distinct advantage of finding the exact solution. In comparison, the **P** found by the linear regression algorithm would be in error by some degree due to the non-linearities. However, in practice it is not possible to exactly represent the T_B versus **P** relationship in terms a model function F(**P**). For example, the T_B not only depends on the columnar content of water vapor but also on vertical distribution of the vapor. Thus, some approximations need to be made when going from the integral equations of radiative transfer to a simplified model function F(**P**). These assumptions were discussed in length in Section 2. In the derivation of the linear regression algorithm, the complete integral formulation of the radiative transfer theory is used, and there is no need for the simplifying assumptions.

In comparing the two types of algorithms, there is a tradeoff between errors due to non-linearities in the linear regression algorithm and errors due to simplifying assumptions in the non-linear, iterative algorithm. Our plan is to develop and test both types of algorithms in parallel, compare their relative performance, and then select one or the other.

3.5. Post-Launch *In-Situ* Regression Algorithm

After AMSR is launched, purely statistical algorithms can be developed by collocating the AMSR T_B's with selected *in-situ* sites. A simple least-squares regression is then found that relates the *in situ* parameter to the T_B's. The mathematical form of this type of algorithm is identical to the linear regression algorithm given by (72). The difference is that the c_{ij} coefficients are not derived from radiative transfer theory, but rather from the regression to the *in situ* data. Examples of this type of algorithm are the *Goodberlet et al.* [1989] SSM/I wind algorithm and the *Alishouse et al.* [1990] SSM/I water vapor algorithm.

The strength of the purely statistical algorithm is that it does not require a radiative transfer model, and hence it is not affected by modeling errors. The weaknesses are:

1. The algorithm for AMSR cannot be developed until after launch.

2. Large *in situ* data sets covering the full range of global conditions must be assembled and collocated with the AMSR observations.

3. The purely statistical algorithm is keyed to specific sensor parameters such as frequency and incidence angle. For example, none of the algorithms developed for SSM/I can be applied to AMSR. In contrast, SSM/I algorithms based on radiative transfer theory can be interpolated to the new AMSR frequencies and incidence angle.

4. Cross-talk among the various geophysical parameters is a problem for the statistical algorithm. For example, consider sea-surface temperature T_S and water vapor V which are highly correlated on a global scale. A purely statistical algorithm will mimic this correlation and will generate a T_S product that is always highly correlated with V. In nature, when the true V changes and T_S remains constant (i.e., a weather system passing by), the statistical algorithm will erroneously report a change in T_S.

5. For the case of cloud water retrieval, for which there is no reliable *in situ* data, this type of algorithm cannot be used.

We think it is a mistake to ignore the physics when developing an algorithm. It may be the case that relatively simple regressions can be used to retrieve some of the parameters. However, it is important that these regressions be understood in the context of radiative transfer theory. Thus, after AMSR is launched and the collocated *in situ* data are available, we will calibrate the pre-launch algorithm by making small adjustments to the radiative transfer model rather than developing purely statistical algorithms. This calibration activity is discussed in the Section 5.

3.6. Incidence Angle Variations

The retrieval of sea-surface temperature and wind speed are sensitive to incidence angle variations. A 1° error in specifying θ_i produces a 6 C error in T_S and a 5 m/s error in W. Thus, it is crucial that the incidence angle be accurately known and that the retrieval algorithm accounts for incidence angle variations.

The pointing knowledge for the PM platform is specified to be 0.03°/axis. This figure is the 3-standard deviation error in the knowledge of the roll, pitch, and yaw. Yaw variations do not affect the incidence angle, but roll and pitch do. The corresponding 3-standard deviation error in incidence angle is approximately 0.05°. The retrieval accuracy for the geophysical parameters are in terms of a 1-standard deviation error, so we convert the incidence angle error to a 1-standard deviation error of 0.016°, and this results in a 0.1 C error in the T_S retrieval and a 0.1 m/s error in the W retrieval. The specification of pointing knowledge for the PM platform is, therefore, sufficient. However, the pointing knowledge of the AMSR instrument is yet to be specified. We will be paying close attention to this instrument specification.

In the non-linear, iterative algorithm, incidence angle is an explicit parameter in the model function, and hence θ_i variations are easily handled by simply assigning a value to θ_i before doing the inversion process. There are two possible methods for handling incidence angle variation in the linear regression algorithm. First, include incidence angle as an additional term in the regression or second, normalize the T_B's to some constant incidence angle, say 55°, before applying the regression. This normalization is expressed by

$$T_B(55^\circ) = T_B(\theta_i) + \mu\,(\theta_i - 55^\circ) \tag{83}$$

where μ represents the derivative $\partial T_B/\partial\theta_i$, which depends on the T_S, W, V, and L. We find that μ can be accurately approximated by a T_B regression of the type given by (73). This method works well when the incidence angle variations are ± 1° or less, which should be the case for AMSR.

4. Level-2 Data Processing Issues

4.1. Retrievals at Different Spatial Resolutions

Figure 7 shows the data processing done by the Level-2 ocean algorithm. The input is the Level-1C data files, which contain brightness temperatures at four base resolutions:

1. Low (L): 6.9 GHz antenna pattern, approximately 58 km resolution
2. Medium (M): 10.7 GHz antenna pattern, approximately 38 km resolution
3. High (H): 18.7 GHz antenna pattern, approximately 24 km resolution
4. Very High (VH): 36.5 GHz antenna pattern, approximately 13 km resolution

For each resolution, all higher frequency channels are averaged down to the base resolution. In this way, all channels within a base resolution set are at a common spatial resolution. The four base resolutions are centered on the observation boresight points, which for AMSR are nearly coincident for all channels other than 89.5 GHz. The ocean algorithm does not use 89.5 GHz. The boresight points are spaced 10 km along the scan, and the scans are separated by 10 km in the along-track direction. For the H and VH resolutions, the Level-1C data set contains T_B's for every boresight point. That is to say, the H and VH Level-1C T_B's are on a 10-km scan-oriented grid system. For the L and M resolutions, a sparse grid that corresponds to every other observation along a scan and every other scan is used for Level-1C. Thus the L and M grid has a 20-km spacing.

The data processing is done by separate modules that correspond to the L, M, V, and VH resolutions. Since the T_S retrievals require the 6.9 GHz channel, the L module's function is find T_S. There is some T_S sensitivity at 10.7 GHz, and as a special product, the M module finds T_S at a higher resolution of 38 km. However, the primary function of the M module is to retrieve wind speed. The H module's primary function is to retrieve the atmospheric parameters V and L. In addition, the H module also computes a high resolution wind, which is a special product. The VH module just retrieves the cloud liquid water parameter, which is used to flag rain.

The four standard products coming from this processing are:

1. Sea-surface temperature at a resolution of 58 km
2. Wind speed at a resolution of 38 km
3. Water vapor at a resolution of 24 km
4. Cloud liquid water at a resolution of 13 km

And the special products are:

1. Sea-surface temperature at a resolution of 38 km
2. Wind speed at a resolution of 24 km

All of these products are output on the 10-km Level-1C grid. This requires that T_S and W, which are retrieved on the 20-km grid, be remapped to the 10-km grid. Thus T_S and W are over-sampled. However, we think using the same output grid for all four parameters is preferable from a user's standpoint, even if some parameters are over-sampled.

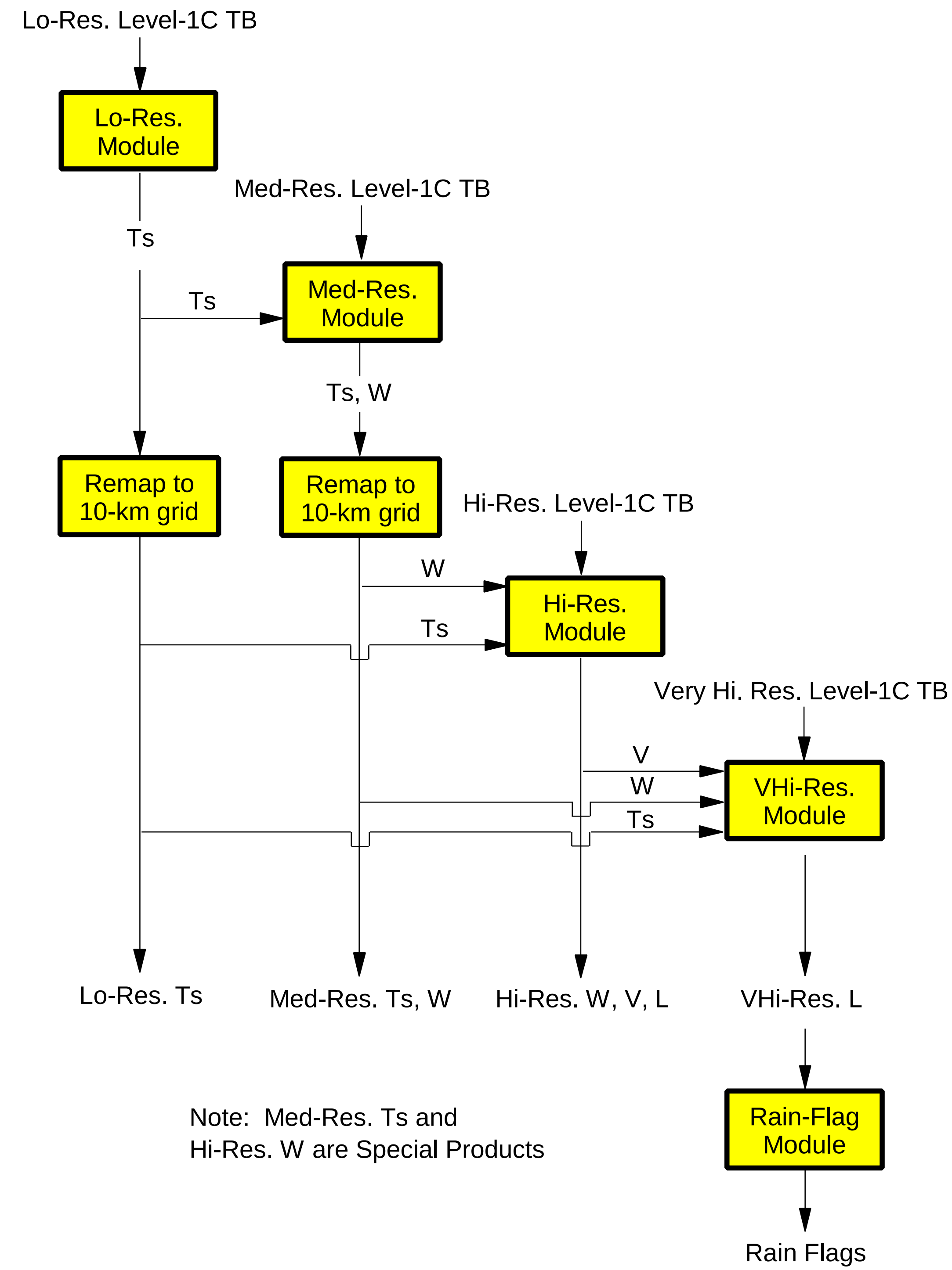

Fig. 7. Data processing flow for ocean algorithm

The first step in the data processing is to compute sea-surface temperature T_S. This is done by the L module which executes the retrieval algorithm described in the previous section. The baseline version of the algorithm uses all AMSR channels except the 89 GHz channels. Later, we may trim down the number of channels if our sensitivity analysis indicates certain channels are not needed. Note that the non-linear, iterative algorithm simultaneously finds W, V, and L along with T_S, but these other retrievals are recomputed at higher spatial resolutions by modules M, H, and VH.

The second step is to compute the medium resolution wind speed, which is done by module M. In this case, only the 10.7 18.7, 23.8, and 36.5 GHz channels are used. Module M also retrieves T_S at the spatial resolution of 38 km. This higher resolution T_S is a special product and will only be useful when the sea-surface temperature is above 15 C. For cold water, the 10.7-GHz $\partial T_B/\partial T_S$ is too small to retrieve T_S. In order to compute W, module M requires the T_S retrieval from module L. For the linear regression algorithm, the T_S retrieval is included as an additional term in the regression for W. For the non-linear, iterative algorithm, the information of the T_S retrieval is included as an additional equation:

$$T_S = \hat{T}_S + \varepsilon_{T_S} \tag{84}$$

where T_S is the higher resolution sea-surface temperature, $\hat{T}_S$ is the estimated lower resolution T_S coming from module L, and ε_{T_S} is the rms error of the estimate. Equation (84) provides the means to vary the way in which $\hat{T}_S$ is assimilated. For example, in cold water, ε_{T_S} can be set to zero (or near zero), which forces the algorithm to retrieve a value of T_S that equals the low resolution value. This is a good choice for cold water because $\partial T_B/\partial T_S$ at 10.7 GHz is too small to retrieve T_S. In warm water, ε_{T_S} can be set to 1 or 2 C. In this case, the algorithm is allowed to retrieve a high resolution T_S that is not necessarily the same as the low resolution T_S, but which is constrained to be relatively close to the low resolution value. This is an example of the flexibility and adaptability of the non-linear algorithm.

The high resolution module is then executed. Module H retrieves the columnar water vapor V and columnar liquid water L. In addition, a high-resolution wind speed is also found. Module H only uses the 18.7, 23.8, and 36.5 GHz channels. The module requires the sea-surface temperature and wind estimates coming from modules L and M. The T_S and W estimates are assimilated into module H in a manner analogous to the way the T_S estimate is assimilated into module M.

The very high resolution 36.5 GHz observations are then processed by module VH. In this case, module VH only finds the cloud liquid water L. The spatial resolution of these retrievals is 13 km. The retrieval algorithm requires the estimates of T_S, W, and V from modules L, M, and H.

The final step is to perform rain flagging. The rain-flag module searches for rain within the L, M, and H footprints. The VH retrievals of L are used as an indicator of rain. Past investigations [*Wentz*, 1990; *Wentz and Spencer*, 1997] have shown that a threshold of L = 0.18 mm is a reliable indicator of rain. The amount of rain in each of the three footprints is determined and the appropriate flag is set. The rain-flag module must search over 15 AMSR scans in order to cover the L footprint out to the first null of the antenna pattern.

4.2 Granules and Metadata

The Level-2 ocean products that are produced for each 1.5-second AMSR scan are listed in Table 10. There are 192 observations taken each scan. The products are stored as unsigned 2-byte positive integers, except for time, that is stored as an 8-byte integer and the orbit number (which includes a fractional part) that is stored as a 4-byte integer. To convert the integers to geophysical units, they are multiplied by the scale factor and then the offset is added. The data rate is 18,496 bits/second, which is 14 megabytes (MB) per orbit or 200 MB/day.

The various Level-2 ocean products are closely tied together, and we therefore define a granule of ocean data as one orbit of all the parameters listed in Table 10. Time and location information are always required for each product. The incidence angle and azimuth angles are included so that corrections can be applied to the products after Level-2 processing. For example, if wind direction variability proves to be a problem for the T_S retrieval (see next section), then a wind-direction database can be later used to correct the problem. The Earth azimuth angle will be required to perform this correction. The four geophysical retrievals are interrelated. Many science applications such as air-sea interaction studies require all four parameters. Also, the atmospheric parameters V and L provide information on the accuracy of the sea-surface parameters T_S and W. Thus we think all of these parameters should be stored together as one granule.

A full description of each product will be included as metadata attached to the granule. The metadata defines each product, provides advice on using the products, and discusses the accuracy and limitations of the products. For example, the metadata will point out that the sea-surface temperature and wind speed retrievals will be of degraded accuracy when rain is present.

Table 10. AMSR Level-2 Ocean Data Record

Data Item	No. Samples	No. Bits	Scale Factor	Offset
Time (sec)	1	64	1	0.0
Orbit Number	1	32	1	0.0
Earth incidence angle (deg)	192	3072	0.01	0.0
Earth azimuth angle (deg)	192	3072	0.01	0.0
Latitude (deg)	192	3072	0.01	0.0
Longitude (deg)	192	3072	0.01	0.0
Surface type and QC flag	192	3072	1	0.0
Sea-Surface Temperature T_S (K)	192	3072	0.01	-5.0
Wind Speed W (m/s)	192	3072	0.01	-4.0
Water Vapor V (m/s)	192	3072	0.01	-2.0
Cloud Liquid Water L (mm)	192	3072	0.001	-0.1
Total bits in record		27744		

4.3. Requirements for Ancillary Data Sets

The AMSR data processing has minimal requirements for ancillary data sets, with one possible exception: wind direction information. If the error in the T_S retrieval due to wind direction variations proves to be unacceptably large, then a wind direction database will be required. This possibility is discussed below. All other ancillary data sets are small static tables that are easily implemented. These data sets are listed in Table 11.

The land-coast-ocean mask is a map that indicates a particular location is either all land, all ocean, or mixed land and ocean. This map is used to exclude observations that are contaminated by the hot thermal emission of land. The sea-surface temperature climatology is used for retrieving W, V, and L when the T_S retrieval from the 6.9 GHz channels is not available. For example, a retrieved value of T_S is not available near coasts and in rainy areas. The sea-surface salinity map is required for the accurate retrieval of T_S. In the open ocean, the salinity varies from about 32 to 37 parts/thousand. The 6.9 GHz v-pol channel is most sensitive to salinity variations. In warm water a 5 parts/thousand change in salinity corresponds to a 0.3 K change in the 6.9V T_B. To achieve a rms accuracy of 0.5 C in the T_S retrieval, the salinity will need to be known to an accuracy of about 2 parts/thousand. The sea-ice climatology mask indicates when a particular location is in an area of possible sea ice. This ice mask is based on 20 years of microwave radiometer (SMMR and SSM/I) sea ice observations. The 20-year maximum extent of sea ice was determined, and then a 100-km buffer was added to ensure that observations outside the mask would be free of ice. The one exception is the occasional large iceberg that moves outside the ice mask. The ice mask is used as a quality control measure to flag retrievals that may be contaminated by emission of sea ice.

Table 11. Ancillary Data Sets Required by Level-2 Ocean Algorithm

Parameter	Temporal Resolution	Spatial Resolution	Source
Land-Coast-Ocean Mask	not applicable	0.1° lat. by 0.1° long.	C.I.A.
Sea-Surface Temperature Climatology	monthly	2° lat. by 2° long.	Shea et al. [1990]
Sea-Surface Salinity Climatology	monthly	2° lat. by 2° long.	To be determined
Sea Ice Climatology Mask	monthly	1° lat. by 1° long.	SSM/I Analysis

Wind direction variability is a major source of error in the T_S retrieval. The simulation studies discussed in Section 3.3 indicate that in the absence of wind direction variability, T_S can be retrieved to an accuracy of 0.3 C. When wind direction variability is included in the simulation, the rms error goes up to 0.6 C. Currently, there is considerable uncertainty of the magnitude of the wind direction T_B signal at 6.9 GHz. The upcoming flights of the TRMM 10.7-GHz radiometer and the ADEOS-2 AMSR will provide valuable information on the wind direction T_B signal at the lower frequencies. If the wind direction variation of the 6.9- GHz T_B proves to be a dominant source of error, then we will need to make a correction to the T_S retrieval based on some wind direction database. There are two possible sources of wind direction information. First is NMC and ECMWF surface analyses, and the second is the SeaWind scatterometer.

4.4. Computer Resources and Programming Standards

The Level-2 processing of the ocean algorithm will require modest computer resources. The SSM/I Level-2 processing can be used as a benchmark. The SSM/I Level-2 processing is done on a Pentium Pro-200™ at Remote Sensing Systems. It takes about 1 day to process one-month of SSM/I data. The AMSR Level-2 processing should be no more than a factor of 10 greater than that for SSM/I. We expect that desktop workstations will continue to increase in performance at a rate of doubling every 2 years. Thus, in the year 2001 when the PM-AMSR data becomes available, we expect that a state-of-the-art desktop workstation will be able to process one-month of AMSR data in one day.

The Level-2 processing will ingest one complete orbit of Level-1C data, excluding the 89.5 GHz observations. This will require about 50 megabytes (MB) of memory to store the input data and 30 MB to store the output data. An additional 64 MB will be more than enough for code, tables, and temporary storage. Thus, a workstation with 256 MB of memory will be more than adequate.

The source code for the algorithm will be written in Fortran 90, and all required SDP Toolkit functions will be implemented.

5. Validation for the Ocean Products Suite

5.1. Introduction

The final, prelaunch ocean algorithm for the EOS-PM AMSR will have benefited from three separate calibration and validation activities: SSM/I, TMI, and ADEOS-2 AMSR. Given this heritage, we expect that the prelaunch AMSR algorithm will perform very well and will provide the scientific community with accurate ocean products. However, there are two caveats that need to be considered. First, it is not possible to absolutely calibrate satellite microwave radiometers to better than 1 to 2 K. In other words, there will probably be a constant T_B bias of 1 to 2 K between SSM/I, TMI, and the two AMSR's. Fortunately, this bias is easily modeled in terms of either an additive or multiplicative offset for each channel. Thus the first caveat is that T_B offsets need to be derived after launch before accurate retrievals can be realized. The second caveat is that some fine tuning of the model coefficients will probably be required in order to maximize the retrieval accuracy.

Given these caveats, we have developed a two-step post-launch calibration/validation (cal/val) plan. First, in order to determine the T_B offsets, we will perform a 2-month, quick-look cal/val. The objective of the 3-month cal/val is to quickly implement the T_B offsets so that reasonably accurate ocean products can be delivered to the scientific community soon after launch. Also, the quick-look calibration may identify other obvious problems in the algorithm that can be corrected. A more thorough 1-year investigation will then be conducted, a precision calibration will be done, and the algorithm will be updated. The updated algorithm will represent the Version 1 post-launch AMSR algorithm, and we anticipate that it will be used to process data for several years. Once the Version-1 software is implemented, we will begin several research activities aimed towards extracting the maximum information content from the AMSR observations. Our AMSR investigation will conclude with an optimal algorithm for retrospective processing of the AMSR data.

The calibration and validation of the first 3 ocean products (T_S, W, and V) will be based on intercomparisons with buoy and radiosonde observations and on T_S retrievals coming from IR satellite sensors. With respect to cloud liquid water, there are no reliable ancillary data sets for calibration or validation. In this case, we will rely on a histogram analysis similar to that done by *Wentz* [1997]. The details of the cal/val activity for each ocean parameter will now be discussed.

5.2 Sea-Surface Temperature Validation

There are two sources of sea-surface temperature (SST) information that will be assembled for the AMSR validation: moored buoy data and T_S retrievals coming from satellite IR sensors. Buoys are frequently used to validate satellite SST measurements even though a satellite measures the ocean skin temperature (temperature of the first millimeter) and buoys measure the ocean bulk temperature. The buoy data are obtained from the National Data Buoy Center (NDBC) and the Pacific Marine Environmental Laboratory (PMEL). NDBC moored buoys measure T_S at a depth of one meter. The hourly measurements are available by anonymous ftp from NDBC in near real time. The Tropical Ocean Global Atmosphere (TOGA)/Tropical Atmosphere-Ocean (TAO) array operated by PMEL consists of nearly 70 moored buoys in the equatorial Pacific. These buoys also measure T_S at 1-meter depth. The TAO T_S samples are taken every ten minutes and averaged at the end of each hour. A full day of hourly values will only be available after buoy recovery. These buoy data sets are discussed further in the next section on wind speed validation.

The infrared (IR) satellite sensors, such as the Advanced Very High Resolution Radiometer (AVHRR), benefit from a two-decade heritage of retrieving T_S. They have a proven capability of measuring T_S in the absence of clouds. We will use these T_S retrievals in cloud-free areas to calibrate the AMSR T_S retrievals. Once calibrated in the cloud-free areas, the AMSR T_S retrievals will also be valid in cloudy areas since non-raining clouds are nearly transparent at 6.9 GHz.

One source of IR T_S retrievals the Multi-Channel SST (MCSST) product derived from AVHRR observations collected at 3.5 to 4 micrometers (AVHRR channel 3) and 10 to 12.5 micrometers (AVHRR channels 4 and 5). This product is shown in Figure 8. The MCSST daily grids are produced by the Naval Oceanographic Office and distributed to NOAA/NESDIS and the Fleet Numerical Meteorology and Oceanography Center. Since clouds are opaque to these wavelengths, and aerosols cause significant scattering, MCSST observations represent the average T_S in cloud free and aerosol free ocean areas. Global gridded results at intervals of 12 hours and a spatial scale of 2×2 AVHRR GAC samples (about 8 km^2 area) are produced, while maintaining an accuracy of 0.7 C rms difference between MCSST and collocated drifting buoy T_S measurements (within 4 hours and 25 km).

Daily and monthly global MCSST analyses are prepared at a spatial scale of 100 km. The daily 100-km product will be most appropriate for the AMSR validation effort. The MCSST observations can also be remapped to other spatial and temporal scales in support of missions such as AMSR. For example, under NASA sponsorship, the MCSST observations have been remapped to 18 km and weekly time scale, to match ocean color maps derived from the CZCS.

5.3 Wind Speed Validation

The chosen method of validation for the AMSR wind speed product is by intercomparisons with wind observations of moored buoys deployed in the open ocean. Currently, NDBC maintains approximately 50 moored data buoys distanced greater than 25 km from shore. These buoys measure barometric pressure, wind direction, wind speed, wind gust, air and sea temperature, and wave energy spectra (i.e., significant wave height, dominant wave period, and average wave period). Wind speed and direction is measured during an 8 minute period prior to the hour of report. Exactly when the data is collected prior to report and the height of the anemometer depends on the type of payload on the moored buoy. These buoys are located primarily in the coastal and offshore waters of the continental United States, the Pacific Ocean around Hawaii, and from the Bering Sea to the South Pacific. In addition, there are about 50 coastal C-man stations that report hourly winds averaged over 2 minutes. The quality checked hourly buoy and C-man measurements are available by anonymous ftp from NOAA computers. Table 12 outlines the location of the NBDC moored buoys in service as of July 1996. These locations are mapped in Figure 9.

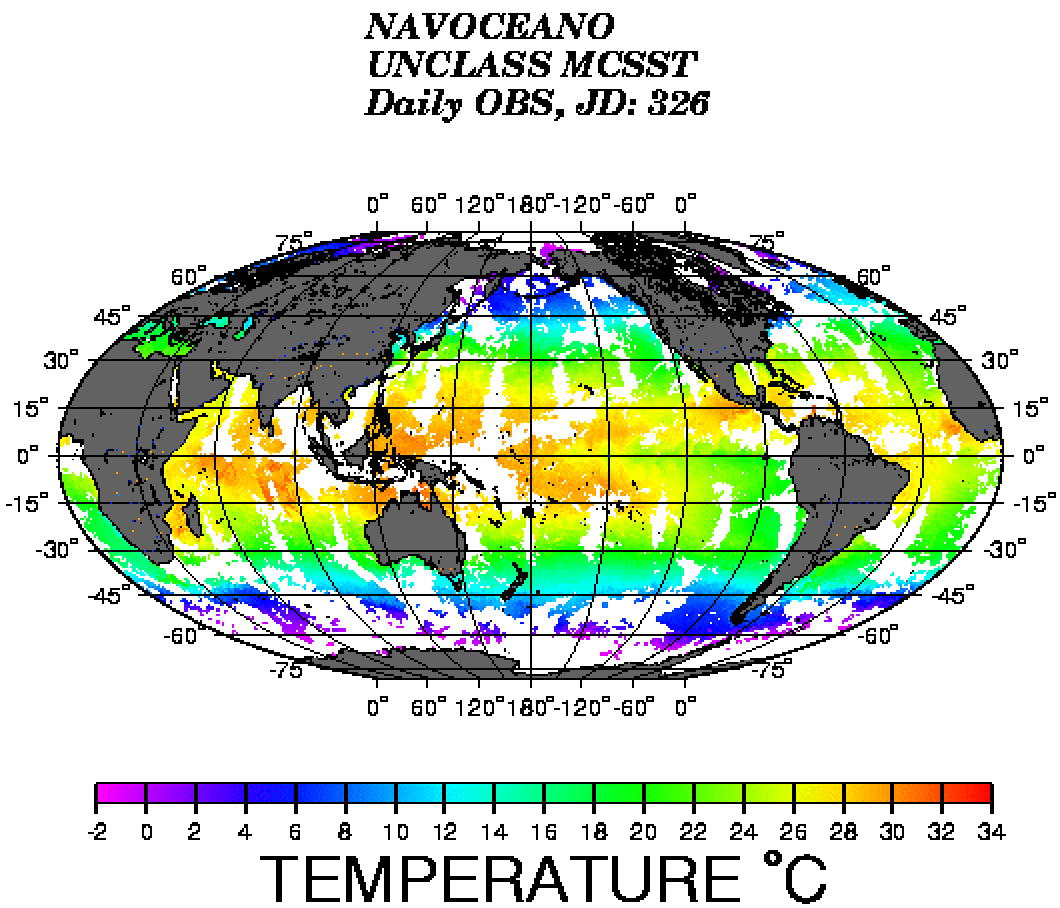

Fig. 8. MCSST Daily Observation Product from Naval Oceanography Center

Table 12. NDBC Moored Buoy Open Water Locations as of July 1996

WMO Number	Latitude	East Longitude	General Location
41001	34.7	287.4	E. Hatteras
41002	32.3	284.8	S. Hatteras
41004	32.5	280.9	E. Charleston
41006	29.3	282.7	E. Daytona
41009	28.5	279.8	Canaveral
41010	28.9	281.5	E. Canaveral
41015	35.4	284.9	Cape Hatteras E
41016	24.6	283.5	Eleuthera
41018	15.0	285.0	Central Caribbean
41019	29.0	289.0	American Basin
42001	25.9	270.3	Mid Gulf of Mexico
42002	25.9	266.4	W. Gulf of Mexico
42003	25.9	274.1	E. Gulf of Mexico
42019	27.9	265.0	Lanelle
42020	27.0	263.5	Eileen
42035	29.2	265.6	Galveston
42036	28.5	275.5	S. Apalachicola
42037	24.5	278.6	Univ. of Miami
42039	28.8	274.0	NE Gulf of Mexico
42040	29.2	271.7	E. Miss River Delta
44004	38.5	289.3	Hotel
44005	42.9	291.1	Gulf of Maine
44006	36.3	284.5	Sandy Duck
44008	40.5	290.6	Nantucket
44009	38.5	285.3	Delaware Bay
44010	36.0	285.0	Sandy Duck
44011	41.1	293.4	Georges Bank
44014	36.6	285.2	Virginia Beach
44019	36.4	284.8	Sandy Duck
44025	40.3	286.8	Long Island
46001	56.3	211.8	Gulf of Alaska
46002	42.5	229.7	Oregon
46003	51.9	204.1	S. Aleutians
46005	46.1	229.0	Washington
46006	40.9	222.5	S.E. Papa
46025	33.7	240.9	Catalina Rdg
46028	35.8	238.1	C San Martin
46035	57.0	182.3	Bering Sea
46050	44.6	235.5	Stonewall Bank
46059	38.0	230.0	Boutelle Seamount
46061	60.2	213.2	Hinchinbrook
46147	51.8	228.8	S. Cape St. James
51001	23.4	197.7	N.W. Hawaii
51002	17.2	202.2	S.W. Hawaii
51003	19.1	199.2	W. Hawaii
51004	17.4	207.5	S.E. Hawaii
51026	21.4	203.1	N. Molokai

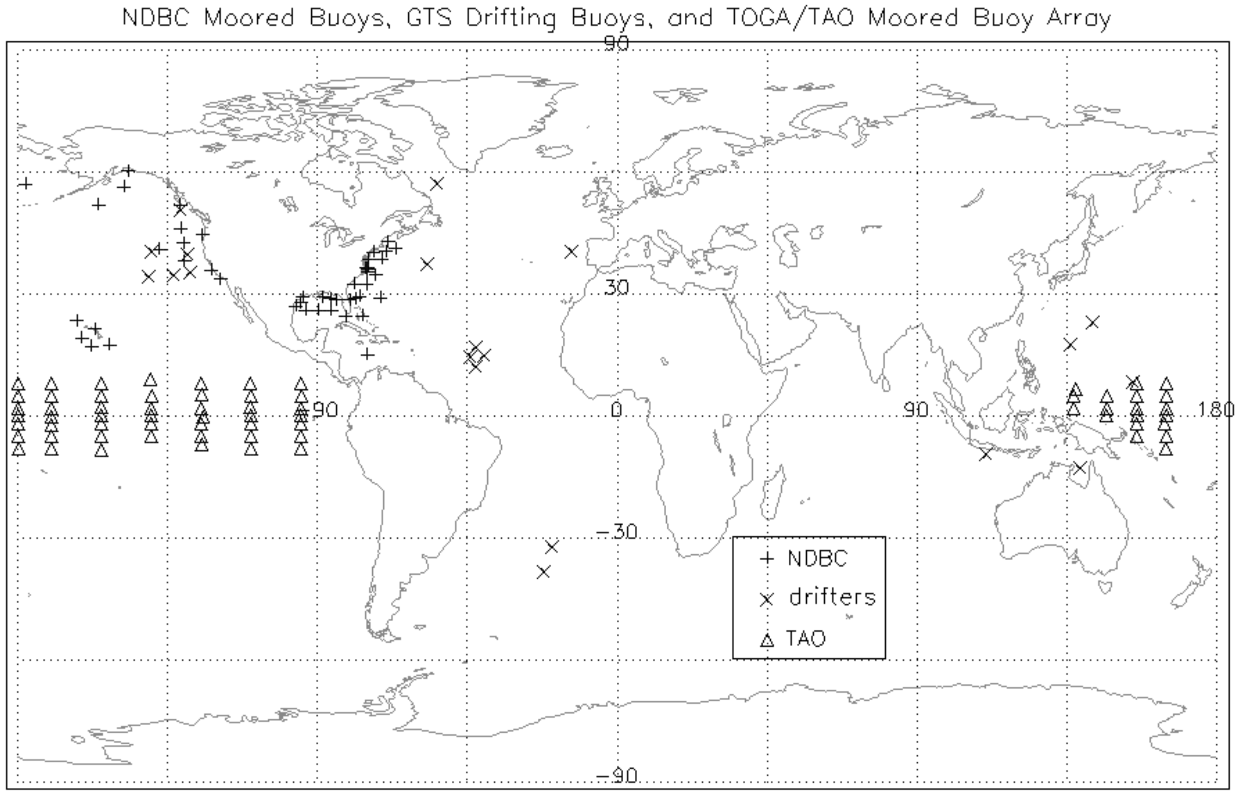

Fig. 9. Locations of data buoys

The 70 moored-buoy TOGA/TAO array covers the tropical Pacific ocean. These buoys are placed at approximately 10 to 15 degree longitude intervals and 2° to 3° degree latitude intervals. They measure air temperature, relative humidity, surface winds, T_S, and subsurface temperature to 500 meters. Wind measurements are made at a height of 4 m for 6 minutes centered on the hour and are vector averaged to derive the hourly value reported. To conserve battery power, hourly data is transmitted only 8 hours each day, 0600 to 1000 and 1200 to 1600 buoy local time. Three to four hours of T_S and wind data are available in near-real time from the GTS. These data are considered preliminary until the buoy is serviced and the stored hourly data is processed. This occurs approximately once each year. Figure 9 includes the TAO buoy network.

The anemometer heights z for the buoys and C-man stations vary. The NDBC moored buoys in general have z equaling 5 or 10 m, but some of the C-man stations have anemometers as high as 60 m. The PMEL anemometers are at 3.8 m above the sea surface. All buoy winds W_B will be normalized to an equivalent anemometer height of 10 m (1000 cm) assuming a logarithmic wind profile.

$$W_{B,10M} = [\ln(1000/h_0)/\ln(h/h_0)]\, W_{B,Z} \tag{85}$$

where h_0 is the surface roughness length, which equals 1.52×10^{-2} cm assuming a drag coefficient of 1.3×10^{-3} [*Peixoto and Oort*, 1992].

The buoy data sets will undergo quality check procedures, including checks for missing data, repeated data, blank fields, and out-of-bounds data. A time interpretive collocation program will calculate the wind speed at the time of the nearest satellite overpass, as is described in *Wentz* [1997].

5.4 Water Vapor Validation

The international radiosonde network will be used to validate the AMSR water vapor product. Radiosonde data are available from several sources, including NMC, NCDC, and NCAR. A radiosonde consists of instruments which measure temperature, pressure, and humidity as they are carried aloft by a helium balloon. In many locations throughout the world radiosondes are launched twice each day (00Z and 12Z). To compare columnar water vapor over ocean regions, only stations on small islands or ships are used. A preliminary list of 56 radiosonde stations currently operating on small islands are listed in Table 13 and are displayed in Figure 10.

Quality control measures will include discarding incomplete or inconsistent soundings, soundings without a surface level report, soundings with fewer than a minimal number of levels, and those with spikes in the temperature or water vapor pressure profiles. These measures will reduce the size of the available data set. In addition, corrections or normalizations among the various types of sensors and sensor configurations will be required since the radiosonde data are from different stations and countries. A collocation program will be used to find the AMSR measurements within a specific space and time of each radiosonde sounding. The details of collocating radiosondes with satellite observation and the associated quality control procedures are given by *Alishouse et al.* [1990] and *Wentz* [1997].

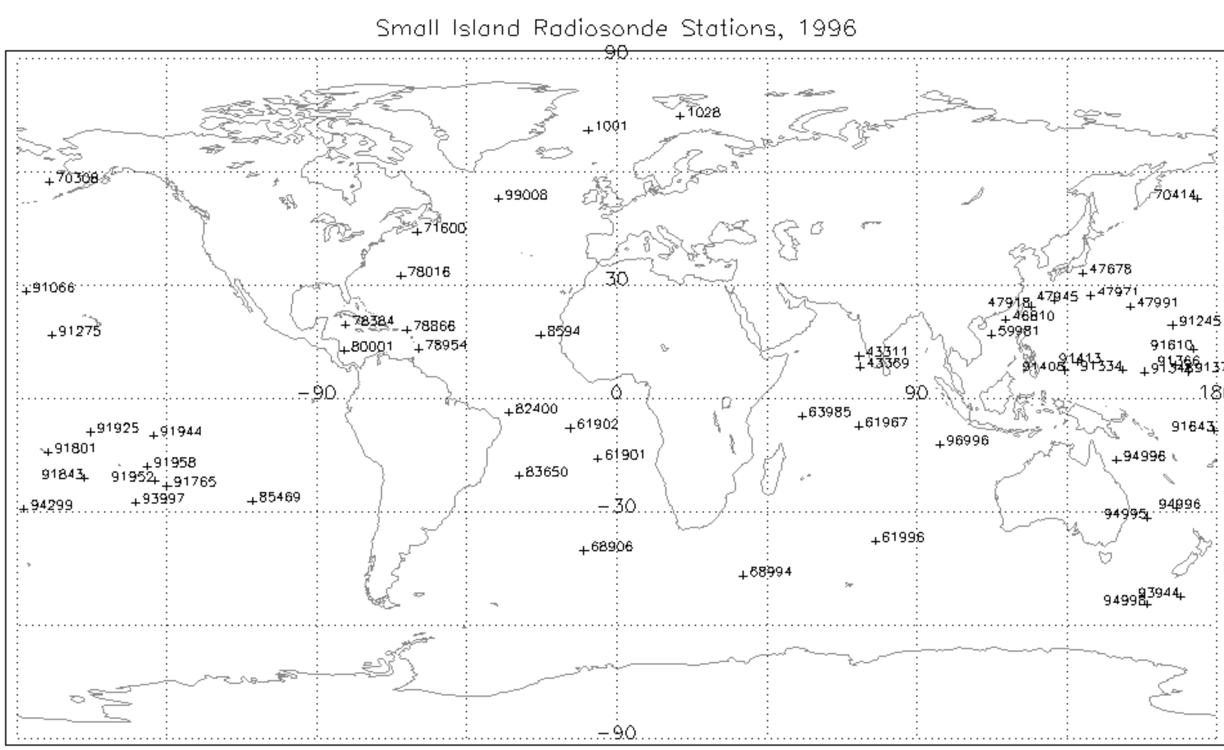

Fig. 10. Radiosonde stations on small islands.

Table 13. Island Radiosonde Station Locations as of September 1996

WMO No.	Name	Latitude	East Longitude	Area (km^2)
1001	JAN MAYEN	70.93	351.33	373
1028	BJORNOYA	74.52	19.02	179
8594	SAL	16.73	337.05	
43311	AMINI	11.12	72.73	
43369	MINICOY	8.30	73.00	
46810	PRATAS IS.	20.70	116.72	
47678	HACHIJA JIMA	33.12	139.78	70
47918	ISHIGAKIJIMA	24.33	124.17	215
47945	MINAMIDAITO JIMA	25.83	131.23	47
47971	CHICHI JIMA	27.08	142.18	25
47991	MARCUS IS.	24.30	153.97	3
59981	XISHA IS.	16.83	112.33	
61901	ST. HELENA	-15.96	354.30	122
61902	ASCENSION IS.	-7.97	345.96	88
61967	DIEGO GARCIA	-7.35	72.48	152
61996	I. N. AMSTERDAM	-37.80	77.53	62
63985	SEYCHELLES INTL	-4.67	55.52	23
68906	GOUGH IS.	-40.35	350.12	83
68994	MARION IS	-46.88	37.87	388
70308	ST. PAUL IS.	57.15	189.79	91
70414	SHEMYA IS.	52.72	174.10	21
71600	SABLE IS.	43.93	299.98	8
78016	KINDLEY FIELD	32.37	295.32	53
78384	ROBERTS FLD.	19.30	278.63	183
78866	SAN MAARTEN	18.05	296.89	85
78954	BARBADOS	13.07	300.50	431
80001	ISLA SAN ANDREAS	12.58	278.30	21
82400	FERNANDO DE NORONHA	-3.85	327.58	4
83650	TRINDADE IS.	-20.50	330.68	10
85469	EASTER IS.	-27.17	250.57	117
91066	MIDWAY	28.22	182.65	15
91245	WAKE IS.	19.28	166.65	8
91275	JOHNSTON IS.	16.73	190.49	1
91334	TRUK	7.47	151.85	118
91348	PONAPE/CAROLINE IS.	6.96	158.22	68
91366	KWAJALEIN	8.72	167.73	16
91376	MAJURO	7.03	171.38	10
91408	KOROR	7.33	134.48	8
91413	YAP	9.48	138.08	54
91610	TARAWA	13.05	172.92	23
91643	FUNAFUTI	-8.52	179.22	3
91765	PAGO PAGO	-14.33	189.29	135
91801	PENRHYN	-9.00	201.95	10
91843	COOK ISLES	-21.20	200.19	218
91925	ATUONA	-9.82	220.99	200
91944	HAO	-18.06	219.05	92
91948	RIKITEA	-23.13	225.04	31
91952	MUROROA	-21.81	221.19	
91958	AUSTRAL IS.	-27.61	215.67	47
93944	CAMPBELL IS.	-52.55	169.15	17
93997	KERMADEC IS	-29.25	182.09	34
94299	WILLIS IS.	-16.30	149.98	
94996	NORFOLK IS.	-29.03	167.93	34
94995	LORD HOWE IS.	-31.53	159.07	2
94998	MACQUARIE IS.	-54.48	158.93	109
96996	COCOS IS.	-12.18	96.82	14

5.5 Cloud Water Validation

Microwave radiometry is probably the most accurate technology for measuring the vertically integrated cloud liquid water L. In the 18 to 37 GHz band, clouds are semi-transparent and the absorption by the entire column of liquid water can be measured. Apart from using upward-looking radiometers to calibrate downward-looking radiometers (or vise versa), there are no other calibration sources for L. Several nations (e.g., The Netherlands) maintain upward looking radiometers or routinely make aircraft flights (e.g., Australia) to measure L in support of their meteorological operations. These data sets are increasingly made available to the scientific community over the Internet. However, the comparison L inferred from upward looking radiometers with that inferred from downward looking satellite radiometers has limited utility. The great spatial and temporal variability of clouds makes such comparisons difficult. Also, the major problem in calibrating L is in obtaining accurate retrievals over the full range of global conditions. There are not enough upward looking radiometers to do this. Finally, when differences arise, it will be difficult to determine which radiometer system is at fault.

We prefer to use the statistical histogram method described by *Wentz* [1997]. This technique is illustrated in Figure 11. We assume the probability density function (pdf) for the true cloud water observed by AMSR has a maximum at L = 0 and rapidly decays similar to an exponential pdf as L increases. The pdf for the retrieved L will look similar, but retrieval error will tend to smear out the sharp peak at L = 0. Simulations in which Gaussian noise is added to a random deviate having an exponential pdf show that the left-side, half-power point of the pdf for the noise-add L is located at L = 0. Thus we require that histograms of the L retrievals are aligned such that the half-power point of the left-side is at L = 0. Furthermore, we require this condition be met for all T_S, W, and V.

For example, the top plot in Figure 11 shows 6 histograms of L retrieved from SSM/I. The 6 histograms correspond to 6 different ranges of T_S (i.e., 0-5 C, 5-10 C, ..., 25-30 C). The middle and bottom plots show analogous results for wind and water vapor groupings. The peak of the pdf's is near L = 0.025 mm. At L = 0, all histograms are about half the peak value. The misalignment among the 6 histograms is about ±0.005 mm. We use the width of this half power point (i.e., 0.025 mm) as an indicator of the rms error in L.

This procedure is effective in eliminating the bias and crosstalk error in the L retrieval, and we consider it the best available way to calibrate the cloud water retrieval.

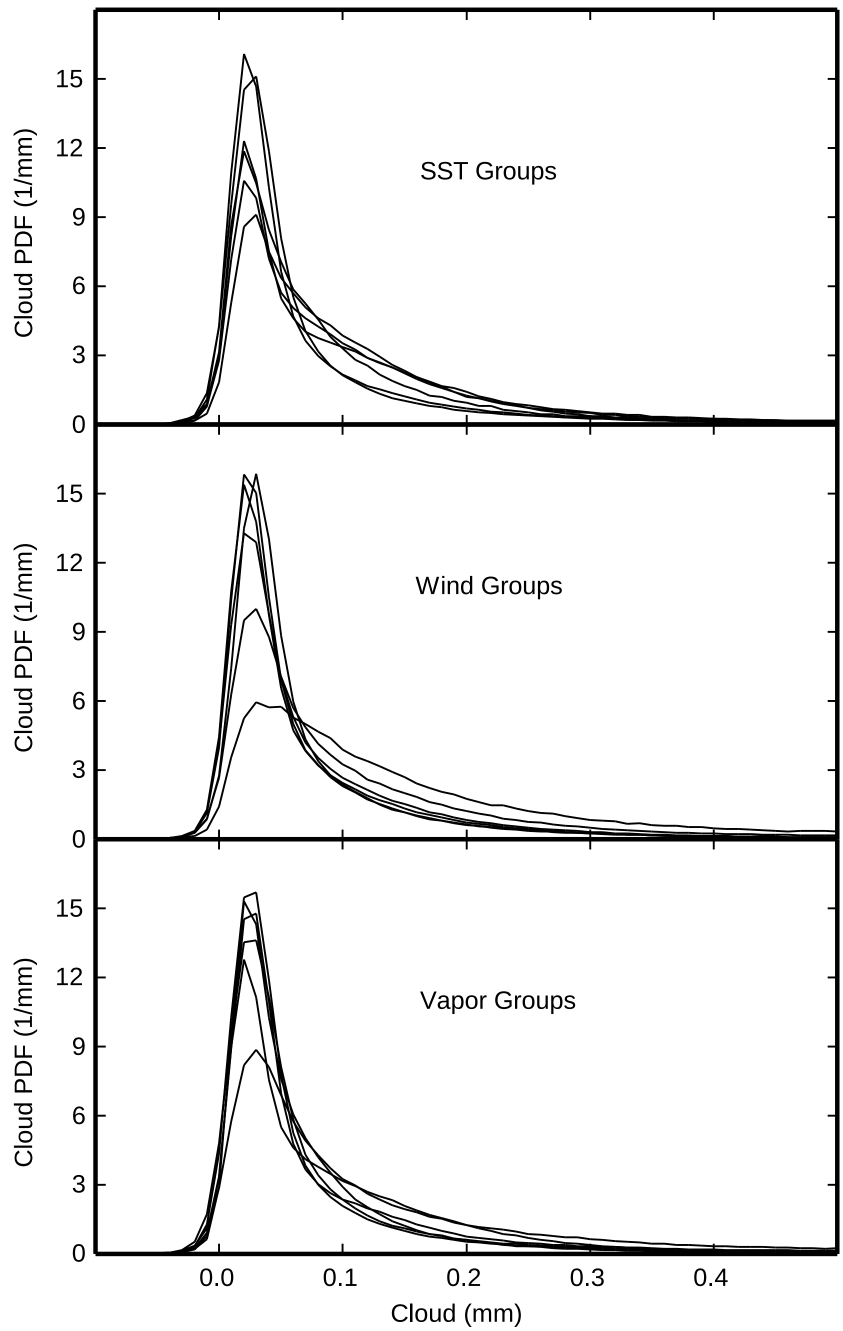

Fig. 11. Probability density functions (pdf) for liquid cloud water. The cloud pdf's are stratified according to sea-surface temperature, wind speed, and water vapor. Each curve shows the pdf for a particular stratification

6. References

Alishouse, J.C., Total precipitable water and rainfall determinations from the SEASAT Scanning Multichannel Microwave Radiometer, *J. Geophys. Res.*, *88*, 1929-1935, 1983.

Alishouse, J.C., S. Synder, J. Vongsathorn, and R.R. Ferraro, Determination of oceanic total precipitable water from the SSM/I, *IEEE Trans. Geoscience and Remote Sensing*, *28*, 811-816, 1990.

Archer, D.G., and P. Wang, The dielectric constant of water and debye-huckel limiting law slopes, *J. Phys. Chem. Ref. Data, 19*, 371, 1990.

Barrett, A.H., and V.K. Chung, A method for the determination of high-altitude water-vapor abundance from ground-based microwave observations, *J. Geophys. Res., 67,* 4259-4266, 1962.

Becker, G.E., and S.H. Autler, Water vapor absorption of electromagnetic radiation in the centimeter wave-length range, *Phys. Rev*., *70*(5/6), 303-307, 1946.

Chang A.T.C., and T.T. Wilheit; Remote Sensing of atmospheric water vapor, liquid water and wind speed at the ocean surface by passive microwave techniques from the Nimbus-5 satellite, *Radio Science, 14*, 793-802, 1979.

Chang, H.D., P.H. Hwang, T.T. Wilheit, A.T.C. Chang, D.H. Staelin, and P.W. Rosenkranz, Monthly distributions of precipitable water from the NIMBUS 7 SMMR data, *J. Geophys. Res*., *89*, 5328-5334, 1984.

Cole, K.S., and R.H. Cole, Dispersion and absorption in dielectrics, *J. Chemical Physics, 9*, 341-351, 1941.

Cox, C.S., Measurements of slopes of high-frequency wind waves, *J. Mar. Res*., *16*, 199-225, 1958.

Cox, C.S., and W.H. Munk, Measurement of the roughness of the sea surface from photographs of the sun's glitter, *J. Opt. Soc. Am., 44*, 838-850, 1954.

Debye, R., *Polar Molecules*, Chemical Catalog, New York, 1929.

Eisberg, R.M., *Fundamentals of Modern Physics*, John Wiley & Sons, Inc., New York, 1961.

Gloersen, P., D.J. Cavalieri, A.T.C. Chang, T.T. Wilheit, W.J. Campbell, O.M. Johannessen, K.B. Katsaros, K.F. Kunzi, D.B. Ross, D. Staelin, E.P.L. Windsor, F.T. Barath, P. Gudmandsen, E. Langham, and R.O. Ramseier, Summary of results from the first NIMBUS 7 SMMR observations, *J. Geophys. Res*., *89*, 5335-5344, 1984.

Goldstein, H., Attenuation by condensed water, *Propagation of Short Radio Waves, MIT Rad. Lab. Ser., 13,* McGraw-Hill, New York: 1951.

Goodberlet, M.A., C.T. Swift, and J.C. Wilkerson, Remote sensing of ocean surface winds with the SSM/I, *J. Geophys. Res., 94*, 14547-14555, 1989.

Grant, E., T. Buchanan, and H. Cook, Dielectric behavior of water at microwave frequencies, *J. Chem. Phys*., *26*, 156-161, 1957.

Grody, N.C., Remote sensing of atmospheric water content from satellites using microwave radiometry, *IEEE Trans. Antennas Propagat., AP-24,* 155-162, 1976.

Haggis, G.H., J.B. Hasted, T.J. Buchanan, The dielectric properties of water in solutions, *J. Chem. Phys., 20*, 1452-1465, 1952.

Hasted, J.B., and S. El Sabeh, The dielectric properties of water in solutions, *Trans. Faraday Soc., 49*, 1003-1011, 1953.

Hasted, J.B., and G. Roderick, Dielectric properties of aqueous and alcoholic electrolytic solutions, *J. Chem. Phys., 29*, 17-26, 1958.

Ho, W., and W. F. Hall, Measurements of the dielectric properties of sea water and NaCl solutions at 2.65 GHz, *J. Geophys. Res., 78*, 6301-6315, 1973.

Ho, W.W., A.W. Love, and M. J. Van Melle, Measurements of the dielectric properties of sea water at 1.43 GHz, *NASA Contractor Report CR-2458*, 1974.

Hollinger, J.P., Passive microwave measurements of sea surface roughness, *IEEE Trans. Geosci. Electron., GE-9,* 165-169, 1971.

Jones, W.L., P.G. Black, D.M. Boggs, E.M. Bracalente, R.A. Brown,, G. Dome, J.A. Ernst, I.M. Halberstam, J.E. Overland, S. Peteherych, W.J. Pierson, F.J. Wentz, P.M. Woiceshyn, and M.G. Wurtele, Seasat scatterometer: Results of the Gulf of Alaska workshop, *Science, 204*, 1413-1415, 1979.

Keller, W.C., and J.W. Wright, Microwave scattering and the straining of wind-generated waves, *Radio Sci., 10*, 139-147, 1975.

Klein, L.A., and C.T. Swift, An improved model for the dielectric constant of sea water at microwave frequencies, *IEEE J. Oceanic Eng., OE-2*, 104-111, 1977.

Lane, J.A., and J.A. Saxton, Dielectric dispersion in pure polar liquids at very high frequencies, III. The effect of electrolytes in solution, Proc. Roy. Soc., A213, 531-545, 1952.

Lide, D.R, *Handbook of Chemistry and Physics, 74th Edition*, CRC Press, Ann Arbor, p. 6-10, 1993.

Liebe, H.J., An updated model for millimeter wave propagation in moist air, *Radio Sci., 20*, 1069-1089, 1985.

Malmberg, C., and A. Maryott, Dielectric constant of water from 0° to 100°C, *J. Res. Nat. Bureau of Standards, 56*, 1-8, 1956.

Marshall, T.S., and W.McK. Palmer, The distribution of raindrops with size, *J. Meteor., 5*, 165-166, 1948.

Milman, A.S. and T. T. Wilheit; Sea surface temperatures form the Scanning Multichannel Microwave Radiometer on Nimbus_7, *J. Geophys Res., 90*, 11631-11641, 1985.

Mitsuyasu, H., and T. Honda, Wind-induced growth of water waves, *J. Fluid Mech., 123*, 425-442, 1982.

Monahan, E.C., and I. O'Muircheartaigh, Optimal power-law description of oceanic whitecap coverage dependence on wind speed, *J. Phys. Oceanogr., 10*, 2094-2099, 1980.

Njoku, E.G., and L. Swanson, Global measurements of sea surface temperature, wind speed, and atmospheric water content from satellite microwave radiometry, *Monthly Weather Review, 111*, 1977-1987, 1983.

Nordberg,W., J. Conaway, D.B. Ross, and T.T. Wilheit, Measurement of microwave emission from a foam covered wind driven sea, *J. Atmos. Sci.*, *38*, 429-433, 1971.

Peake, W.H., Interaction of electromagnetic waves with some natural surfaces, *IEEE Trans. Antennas Propagat*., *AP-7*, S324-S329, 1959.

Peixoto, J.P. and A.H. Oort, *Physics of Climate.* American Institute of Physics, New York, 1992.

Reif, F., *Fundamentals of Statistical and Thermal Physics*, McGraw-Hill, Inc., San Francisco, p. 381-388, 1965.

Rice, S.O., Reflection of electromagnetic waves from slightly rough surfaces, *Commun. Pure Appl. Math*, *4*, 351-378, 1951.

Rosenkranz, P.W., Shape of the 5 mm oxygen band in the atmosphere, *IEEE Tran. Antennas Propag*., *AP-23*(4), 498-506, 1975.

Schluessel, P., and H. Luthardt, Surface wind speeds over the North Sea from Special Sensor Microwave/Imager Observations, *J. Geophys. Res*., *96*, 4845-4853, 1991.

Shea, D.J., K.E. Trenberth, and R.W. Reynolds, A global monthly sea surface temperature climatology, *NCAR Tech. Note 345,* National Center for Atmospheric Research, 167 pp, 1990.

Smith, P.M., The emissivity of sea foam at 19 and 37 GHz, *IEEE Trans. Geosci. Remote Sensing*, *GE-26*, 541-547, 1988.

Staelin, D.H., Measurements and interpretation of the microwave spectrum of the terrestrial atmosphere near 1-cm wavelengths, *J. Geophys Res., 71*, 2875-2881, 1966.

Staelin, D.H., K.F. Kunzi, R.L. Pettyjohn, R.K.L. Poon, R.W. Wilcox and J.W. Waters, Remote sensing of atmospheric water vapor and liquid water with the Nimbus-5 microwave spectrometer, *J. Appl. Meteor.,15,* 1204-1214, 1976.

Stogryn, A., The apparent temperature of the sea at microwave frequencies, *IEEE Trans. Antennas Propagat., AP-15,* 278-286, 1967.

Stogryn, A., Equations for calculating the dielectric constant of saline water, *IEEE Trans. Microwave Theory Tech., MTT-19*, 733-736, 1971.

Stogryn, A., The emissivity of sea foam at microwave frequencies, *J. Geophys. Res*., *77*, 1650-1666, 1972.

Waters, J.R., Absorption and emission by atmospheric gases, *in Methods of Experimental Physics*, vol. 12B, edited by M.L. Meeks, chap. 2.3, Academic, Orlando, Fla., 1976.

Webster, W.J., T.T. Wilheit, D.B. Ross, and P. Gloersen, Spectral characteristics of the microwave emission from a wind-driven foam-covered sea, *J. Geophys. Res*., *81*, 3095-3099, 1976.

Wentz, F.J., A two-scale scattering model for foam-free sea microwave brightness temperatures, *J. Geophys. Res., 80,* 3441-3446, 1975.

Wentz, F.J., A model function for ocean microwave brightness temperatures, *J. Geophys. Res., 88,* 1892-1908, 1983.

Wentz, F.J., L. A. Mattox, and S. Peteherych, New algorithms for microwave measurements of ocean winds: Applications to SeaSat and the Special Sensor Microwave Imager, *J. Geophys. Res., 91*, 2289-2307, 1986.

Wentz, F.J., SBIR phase II report: West coast storm forecasting with SSM/I, *RSS Tech. Rpt. 033190*, Remote Sensing Systems, Santa Rosa, Ca, 378 pp., 1990.

Wentz, F.J., Measurement of oceanic wind vector using satellite microwave radiometers, *IEEE Trans. Geosci. and Remote Sensing, 30,* 960-972, 1992.

Wentz, F.J., A well-calibrated ocean algorithm for SSM/I, *J. Geophys. Res.,102,* 8703-8718, 1997.

Wentz, F.J., and R.W. Spencer, SSM/I rain retrievals within an unified all-weather ocean algorithm, *J. Atmospheric Science*, *55*, 1613-1627, 1998.

Weyl, P.K., On the change in electrical conductance of sea water with temperature, *Limnol. Oceanogr., 9*, 75-78, 1964.

Wilheit T.T., and M.G. Fowler; Microwave radiometric determination of wind speed at the surface of the ocean during BESEX, *IEEE Trans. Antennas Propagat., AP-25,* 111-120, 1977.

Wilheit T.T., The effect of wind on the microwave emission from the ocean's surface at 37 GHz, *J. Geophys. Res., 84*, 4921-4926,1979a.

Wilheit T. T.; A model for the microwave emissivity of the ocean's surface as a function of wind speed, *IEEE Trans. Gesoci. Electronics, GE-17,* 244-249, 1979b.

Wilheit, T.T., and A.T.C. Chang, An algorithm for retrieval of ocean surface and atmospheric parameters from the observations of the Scanning Multichannel Microwave Radiometer (SMMR), *Radio Science, 15,* 525-544, 1980.

Wu, S.T., and A.K. Fung, A non-coherent model for microwave emission and backscattering from the sea surface, *J. Geophys. Res., 77,* 5917-5929, 1972.